bioRxiv preprint doi: https://doi.org/10.1101/156422; this version posted June 27, 2017. The copyright holder for this preprint (which was not certified by peer review) is the author/funder. All rights reserved. No reuse allowed without permission.

Title:

Artificial anion-conducting channelrhodopsins with tuned spectra, modified kinetics and enhanced light sensitivity

Authors:

Jonas Wietek[a], Silvia Rodriguez-Rozada[d,1], Janine Tutas[b,1], Federico Tenedini[b], Christiane Grimm[a], Thomas G. Oertner[c], Peter Soba[b], Peter Hegemann[a], J. Simon Wiegert[c,d,2]

Affiliations:

a) Institute for Biology, Experimental Biophysics, Humboldt-Universität zu Berlin, Invalidenstraße 42, 10115 Berlin, Germany.

b) Research Group Neuronal Patterning and Connectivity, Center for Molecular Neurobiology Hamburg, Falkenried 94, 20251 Hamburg, Germany.

c) Institute for Synaptic Physiology, Center for Molecular Neurobiology Hamburg, Falkenried 94, 20251 Hamburg, Germany.

d) Research Group Synaptic Wiring and Information Processing, Center for Molecular Neurobiology Hamburg, Falkenried 94, 20251 Hamburg, Germany

1) Equal contribution

2) Correspondence to: simon.wiegert@zmnh.uni-hamburg.de, phone: +49 40 7410 55354

Keywords:

optogenetics, neuronal silencing, anion-conducting channelrhodopsin, channel engineering, hippocampal neurons, Drosophila melanogaster, animal behavior

bioRxiv preprint doi: https://doi.org/10.1101/156422; this version posted June 27, 2017. The copyright holder for this preprint (which was not certified by peer review) is the author/funder. All rights reserved. No reuse allowed without permission.

Genetic engineering of natural light-gated ion channels has proven a powerful way to generate optogenetic tools for a wide variety of applications. In recent years, blue light-activated artificial anion conducting channelrhodopsins (aACRs) have been developed, improved, and were successfully applied *in vivo*. We asked whether the approaches used to create aACRs can be transferred to other well-characterized cation-conducting channelrhodopsins (CCRs) to obtain aACRs with a broad spectrum of biophysical properties. We generated 22 variants using two conversion strategies applied to 11 CCRs and screened them for membrane expression, photocurrents and anion selectivity. We obtained two novel aACRs, Phobos and Aurora, with blue- and red-shifted action spectra and photocurrents similar to existing aACRs. Furthermore, step-function mutations greatly enhanced light sensitivity due to a slowed-down photocycle. These bistable aACRs can be reversibly toggled between open and closed states with brief light pulses of different wavelengths. All new aACRs reliably inhibited action potential firing in pyramidal CA1 neurons. Expressed in *Drosophila* larvae *in vivo*, aACRs conveyed robust and specific light-dependent inhibition of locomotion and nociception.

bioRxiv preprint doi: https://doi.org/10.1101/156422; this version posted June 27, 2017. The copyright holder for this preprint (which was not certified by peer review) is the author/funder. All rights reserved. No reuse allowed without permission.

Introduction:

The discovery of natural anion conducting channelrhodopsins (nACRs) [1-4], and the development of artificial anion-conducting channelrhodopsins (aACRs) by targeted mutagenesis of cation-conducting channelrhodopsins (CCRs) [5-8] introduced a new class of optogenetic tools. The existing aACRs were derived from either *Chlamydomonas reinhardtii* channelrhodopsin-2 (*Cr*ChR2) [8] or the channelrhodopsin chimera C1C2[6] using two complementary strategies. Exchange of a single glutamate for an arginine in the central gate of *Cr*ChR2 was sufficient to invert ion selectivity. Additional exchange of two glutamate residues in the outer pore and the inner gate completely eliminated residual proton conductance, yielding the highly anion-selective aACR iChloC[7]. In parallel, Berndt *et al.* mutated several amino acids within C1C2 to render the electrostatic potential of the conducting pore more positive, which strongly favored anion conductance[6]. Further improvements led to the highly anion selective aACR iC++ and the related step function version SwiChR++[5]. These improved versions have been successfully used to silence neurons in mice *in vivo* [5,7,9-12].

We asked whether the approaches used to create aACRs can be transferred to other known CCRs to obtain aACRs with a broad spectrum of biophysical properties, especially different kinetics and spectral sensitivities. So far, all aACRs show action spectra similar to *Cr*ChR2 with maximal activation in the blue light range. ACRs with a red-shifted absorption maximum are desirable mainly for three reasons: First, long-wavelength light penetrates deeper into biological tissue due to lower absorption and scattering [13,14]. This enables silencing of larger volumes at reduced light energies compared to blue-light activated tools [15]. Second, combination with blue-light activated tools becomes possible. Third, many animals are blind to light beyond ~600 nm, while visible light exposure can result in positive or negative phototaxis, particularly in invertebrates [16,17]. Red light activation avoids or reduces direct effects of the light pulse on behavior. On the other hand, aACRs with a blue-shifted action spectrum could be useful in combination with red-shifted sensors and actuators, as their excitation would not interfere with activation of such ACRs.

Adding step-function mutations to spectrally shifted aACRs conveys further benefits: In these mutants, a long-lasting chloride conductance can be activated by a short light pulse and terminated by a second light pulse of longer wavelength [5,18,19]. Due to the extremely slow photocycle, photons are integrated over time, increasing the operational light sensitivity of target cells by orders of magnitude.

Here, we report the successful development of two new aACRs, termed Phobos and Aurora, which express well in neurons and provide sufficient photocurrents for efficient silencing.

bioRxiv preprint doi: https://doi.org/10.1101/156422; this version posted June 27, 2017. The copyright holder for this preprint (which was not certified by peer review) is the author/funder. All rights reserved. No reuse allowed without permission.

Compared to existing aACRs, Phobos and Aurora exhibit blue- and red-shifted action spectra, making them potentially suitable for dual-wavelength experiments with spectrally distinct actuators or sensors of the optogenetic toolbox. Adding the step-function mutation C128A to Aurora, Phobos and the previously published iChloC [7] yielded bi-stable versions which could be toggled between open and closed states with short light pulses.

We characterized the biophysical properties of these new aACRs in HEK cells and verified their silencing ability in organotypic hippocampal slice cultures. Potent aACR variants were further tested in larvae of *Drosophila melanogaster*, an organism where the classical light-activated ion pumps halorhodopsin (NpHR) [20,21] and archaerhodopsin Arch [22] show little effect. In contrast to eNpHR, light-activation of Aurora in nociceptive class IV dendritic arborization (C4da) neurons [23] acutely abolished nociceptive behavioral responses and activation of Aurora or the step-function variant of Phobos in motor neurons reversibly decreased locomotion.

bioRxiv preprint doi: https://doi.org/10.1101/156422; this version posted June 27, 2017. The copyright holder for this preprint (which was not certified by peer review) is the author/funder. All rights reserved. No reuse allowed without permission.

Results:

Biophysical characterization in HEK cells

To obtain new aACRs with distinct spectral and kinetic properties, we aimed at converting well-characterized cation-conducting ChRs with known biophysical properties into anion channels. For this, two distinct, previously successful approaches were taken [5,6,8]. According to the first approach [8], we replaced the central gate glutamate (E90R; *Cr*ChR2) with arginine in various ChRs (Figure 1A, B). The new mutants were expressed in HEK cells and tested for membrane expression and photocurrents. *Ts*ChR^{E72R} (*Tetraselmis striata* ChR) [39], *Ps*ChR2^{E73R} (*Platymonas subcordiformis* ChR2) [40], *Vc*ChR1^{E85R} (*Volvox carteri* ChR1) [41] and Chronos^{E107R} (*Stigeoclonium helveticum* ChR) [39] did not yield detectable photocurrents (Figure 1B, Figure S2A). Because Chronos exhibits no serine at the homologous position of S63, which is a main constituent of the inner gate in *Cr*ChR2 we speculated that a differently arranged inner gate could be responsible for the missing photocurrents. Therefore, we created the double mutant Chronos$^{A80S\ E107R}$ to reconstitute a serine residue at the putative inner gate while rendering the central gate anion conductive. However, this mutant still remained non-functional (data not shown). The chimeric ChRs C1C2^{E129R} [42,43] and C1V1^{E129R} [44,45] showed partial Cl^--conductivity but current amplitudes were below 10 pA and membrane localization was poor (Figure 1B, Figure S2A). The mutated *Tc*ChR (*Tetraselmis cordiformis* ChR) [39] displayed photocurrents, but the reversal potential was not shifted upon change of the Cl^- gradient (Figure 1B, Figure S2A). In case of the red shifted ChRs Chrimson (*Chlamydomonas noctigama* ChR1) [39] and ReaChR [46] the E90R homologous mutation caused reduction of photocurrents and a strong reduction of the channel closing time constant. However, again no (Chrimson) or only minor (ReaChR) shifts of the reversal potential upon change of the Cl^- gradient were detected (Figure 1B, Figure S2 A). The only ChR that could be converted was the highly *Cr*ChR2-related *Co*ChR (Figures 1B, S2A and S10) from *Chloromonas oogama* [5,39]. As shown previously, additional introduction of the iChloC homologous mutations (*Co*ChR E63Q E70R E81S) further improved the Cl^--selectivity (Figures 1B, S3) but neuronal expression revealed toxic side effects [7]. Because the ChloC conversion strategy (i.e. to replace the homologous glutamate 90 in the inner gate) was not generalizable to other ChR variants, we proceeded with the second approach and transferred the mutations and the N-terminal sequence from the aACR iC++ [5] to the same group of ChRs (Figure 1A, B). Most constructs (*Tc*ChR, *Ts*ChR, *Ps*ChR2, [40] Chronos and Chrimson) showed no photocurrents and only weak expression and/or membrane localization (Figure S2B). As with the ChloC strategy, *Cr*ChR2 and *Co*ChR could be successfully converted and showed high Cl^--selectivity. However, both variants showed no improvements compared to iC++ (Figures 1B, S2B) and were not further investigated.

bioRxiv preprint doi: https://doi.org/10.1101/156422; this version posted June 27, 2017. The copyright holder for this preprint (which was not certified by peer review) is the author/funder. All rights reserved. No reuse allowed without permission.

Conversion of the red-shifted ChRs [41] was also successful, but the converted *Vc*ChR1 and C1V1 showed photocurrents below 10 pA. In contrast, the modified ReaChR displayed robust current amplitudes upon illumination with green light, which were comparable to iC++ photocurrents evoked by blue-light (Figures 1E, S2B). Thus, both engineering strategies previously used to generate iChloC and iC++ are not generally applicable to convert cation-conducting ChRs into aACRs. Only *Cr*ChR2, *Co*ChR and ReaChR were successfully transformed with the iC++-based strategy. ReaChR, due to its red-shifted action spectrum, is a promising new candidate for a green/yellow/red light activated ACR. Since no ChR with blue-shifted absorption (*Tc*ChR, *Ts*ChR and *Ps*ChR2) could be successfully converted, we aimed to shift the absorption of iC++ by introducing the mutations T159G and G163A that are present in all three deep-blue absorbing ChRs [39]. These mutations induced a blue-shift when the homologous mutations were used in the parental C1C2 construct [47]. The double mutant iC++$^{T159G\ G163A}$ indeed showed blue-shifted maximal activity (Figure 1C) without altering photocurrent amplitudes and membrane expression compared to iC++ (Figures 1D, S2B).

In summary, our screen of 22 different putatively anion-selective constructs yielded two functional aACRs with novel properties, namely the blue-shifted iC++$^{T159G\ G163A}$, which we termed Phobos and the red-shifted anion-selective ReaChR variant, which we termed Aurora.

We next characterized the biophysical properties of Phobos and Aurora in HEK cells alongside the two established aACRs iC++ and iChloC. Phobos showed photocurrent properties similar to the parental iC++. Light application evoked fast currents that decayed to a stationary level. After light shutoff the current rapidly decayed to baseline with a time constant of 10.1 ± 0.8 ms (Figure 1D). Aurora, like the parental ReaChR [46], showed higher inactivation and slower *off*-kinetics (264 ± 19 ms). As previously demonstrated for ReaChR [46,48], high stationary currents could also be evoked with orange light (590 nm), where no fast peak current is observed, making Aurora suitable for red-shifted activation (Figure 1E).

The action spectrum maxima of the new ACRs were substantially shifted to 467 nm (n = 6, Phobos), and 517 nm (n = 5, Aurora) compared to the maxima of iC++ and iChloC, which were at 488 nm (n = 9) and 494 nm (n = 6), respectively (Figure 1C). Thus, the T159G G163A mutations resulted in a 22 nm blue-shift with respect to the parental iC++. When longer light pulses (500 ms) with 10-fold increased photon irradiance were used, the action spectrum of Aurora broadened, revealing two peaks at 419 nm and 585 nm (n = 6). The central part of the spectrum showed a minimum in the region where the low intensity spectrum was maximal (Figure 1C), possibly caused by inactivation due to absorption of the ground and conducting state in the same spectral range [48].

bioRxiv preprint doi: https://doi.org/10.1101/156422; this version posted June 27, 2017. The copyright holder for this preprint (which was not certified by peer review) is the author/funder. All rights reserved. No reuse allowed without permission.

Next, we aimed to slow down the photocycle of iChloC, Phobos and Aurora to create bi-stable aACRs with high operational light sensitivity [5,18,19]. Previously, introduction of the C128A mutation in iC++ produced a bi-stable aACR called SwiChR++ whose closing kinetics can be accelerated by red light, making it switchable between open and closed conformation with short light pulses [5] (Figure 2D-G). Due to the decelerated photocycle aACRs accumulate the open state, thereby increasing the light sensitivity by several orders of magnitude (Figure 2B, C). Similar to SwiChR++ (here termed iC++^{CA} for consistency), where we measured a 3333-fold slower closing time constant than iC++, our new C128A variants of iChloC, Phobos and Aurora showed 19-fold, 24559-fold, and 1604-fold reductions in their *off*-kinetics, respectively (Figure 2A,F). Light sensitivity and closing time constant were linearly related except for iChloC, which had a slightly elevated light sensitivity compared to its closing time constant (Figure S4B). Aurora (EC_{50} = 0.037 ± 0.003 mW/mm²; n = 5) already showed a higher operational light sensitivity compared to Phobos and iC++ (EC_{50} = 0.22 ± 0.06 mW/mm², n = 5 and 0.21 ± 0.01 mW/mm², n = 6) due to slower off kinetics (Figure 2A-C, F). Furthermore, Aurora and Aurora^{CA} displayed inactivation at high green light intensities (Figure 2B) again indicating secondary photochemistry at high light intensities [48], leading to additional inactivation by light as already seen in the action spectra (Figure 1C). Orange light (590 to 600 nm) could be used to excite Aurora at the second peak (Figure 1C). However, light sensitivity was 14 fold lower compared to 530 nm, but only 2-3 fold lower compared to Phobos or iC++. Upon activation with 490 nm light iC++^{CA} partially inactivated already at medium light intensities, but blue-shifting the activation wavelength abolished partial inactivation (Figure 2B, S4A). The *off*-kinetics of step-function aACRs could be accelerated by light in a wavelength and intensity-dependent manner as reported for other step-function ChR variants [5,18,19,49]. To determine the inactivation spectra of the C128A aACR variants, we applied a second light pulse after step-function aACR activation at different wavelengths with equal photon irradiance (Figure 2D, E). The maximal inactivation of slow-cycling aACRs was found at 589 nm (n = 6, iC++^{CA}/SwiChR++), 603 nm (n = 5, iChloC^{CA}), 580 nm (n = 4, Phobos^{CA}) and 626 nm (n = 5, Aurora^{CA}) (Figure 2E). Maximal additional activation was slightly blue-shifted compared to the parental fast cycling aACRs (Figure 2E).

Full channel closing of slow-cycling aACR variants could be achieved within seconds or less with red-shifted light. For Phobos^{CA} the closing kinetics were accelerated 3 orders of magnitude from 249 ± 10 s (n = 4) to 391 ± 15 ms (n = 5) with 590 nm light. Closing of the iC++ C128A mutation was 115 ± 9 s (n = 7) and could be accelerated 3 orders of magnitude by 600 nm light to 150 ± 15 ms (n = 7), while the Aurora step-function variant C128A could be accelerated from 424 ± 15 s to 916 ± 43 ms (n = 5) with 635 nm light. As light-accelerated closing is a function of light energy, the *off*-kinetics of aACR C128A variants might be further accelerated with more intense red light [49]. We tested this for iChloC^{CA}, where closing could

bioRxiv preprint doi: https://doi.org/10.1101/156422; this version posted June 27, 2017. The copyright holder for this preprint (which was not certified by peer review) is the author/funder. All rights reserved. No reuse allowed without permission.

be accelerated from 128 ± 9 s (n = 5) to 346 ± 20 ms (n = 8) at the maximal intensity available (1.95 mW/mm²) at 610 nm (Figures 2F, S4C, D). With the optimal spectral wavelengths for excitation and inactivation of step-function aACRs, temporally precise toggling between open and closed states becomes feasible (Figure 2G).

Next, we systematically compared the following additional parameters of Phobos, Aurora, iC++ and iChloC and their respective C128A variants in HEK cells: photocurrent amplitude, reversal potential and membrane targeting. First, to determine membrane localization, we imaged mCherry labelled aACRs, in HEK cells labelled with the membrane marker Vybrant® DiO by confocal microscopy. All aACRs showed almost exclusive plasma membrane localization with no or only minor fractions of protein found in intracellular compartments (Figure 3A). The relative membrane targeting was >89 % (n = 11 to 21) for all constructs (Figure 3B). At saturating light intensities (*c.f.* Figure 1D, E) stationary photocurrents of fast-cycling aACRs ranged between 560 and 720 pA, similar to iC++ and two times larger than iChloC. Except for iChloC, all slow-cycling aACR variants had 40 to 60 % smaller current amplitudes compared to their parental constructs (Figure 3C). When activated with 590 nm, which corresponds to the second activation peak, photocurrents of Aurora and Aurora^{CA} reached 69 % of the green light evoked photocurrent. Finally, we verified chloride selectivity by measuring the reversal potential (E_{rev}) for light-evoked photocurrents. E_{rev} varied only minimally between aACRs (-65.1 ± 0.3 mV, n = 5 to 8) confirming their high chloride selectivity (Figure 3D).

Photocurrents and spike inhibition in hippocampal neurons

After biophysical characterization of Aurora and Phobos including their respective step-function variants in HEK cells, we next tested their performance in hippocampal neurons. Citrine-labeled Aurora or Phobos was co-expressed with mCerulean in CA1 pyramidal neurons of organotypic hippocampal slice cultures. Four to five days after single-cell electroporation, transfected neurons could be readily identified by their volume marker mCerulean. CA1 neurons had normal morphology and showed bright, membrane-localized expression of the Citrine-labeled aACRs, indicating proper membrane insertion of the aACRs without any obvious effect on neuronal morphology (Figure 4A, E). In whole-cell patch-clamp experiments we first measured basic biophysical membrane properties of aACR expressing CA1 neurons in the dark. Overexpression of Phobos or Aurora did not alter membrane properties or spiking parameters (Supplementary table 1). We next measured the action spectra of Aurora and Phobos to assess their utility as color-shifted silencing tools in neurons. CA1 neurons were voltage-clamped at -50 mV, approx. 25 mV above the calculated Nernst potential for chloride (-75.9 mV). Under these conditions, entry of Cl^- ions resulted in outward-directed photocurrents. All experiments were done in the presence of blockers of

bioRxiv preprint doi: https://doi.org/10.1101/156422; this version posted June 27, 2017. The copyright holder for this preprint (which was not certified by peer review) is the author/funder. All rights reserved. No reuse allowed without permission.

ionotropic synaptic transmission. Similar to HEK cell experiments, the action spectrum of Aurora was red-shifted and photocurrents showed a fast inactivating component (Figure 4B, S5). Illumination with orange-red light produced photocurrents with a slower onset and lack of the fast component due to reduced absorption cross-section at this wavelength. Tonic photocurrents still reached 57 ± 3 % of the maximal stationary current at 595 nm and 34 ± 4 % at 635 nm. Thus, orange-to-red light is suitable to evoke photocurrents in Aurora-expressing neurons (Figure 4B, S5). To test the ability of Aurora to block action potentials at various wavelengths, we held neurons in current clamp and injected a depolarizing current step of 500 pA for 500 ms, triggering typically 7-15 action potentials (Figure 4C). During current injection, light pulses (200 ms) ranging from 365 nm to 660 nm at intensities of 0.1, 1 and 10 mW/mm^2 were applied. At the lowest light intensity (0.1 mW/mm^2), >80 % of action potentials were blocked between 470 and 525 nm, confirming our HEK cell measurements of Aurora's action spectrum (Figure 4D). Under high-intensity illumination (10 mW/mm^2), however, the spectral range for efficient blocking (>80%) was greatly extended, reaching from 365 to 595 nm (Figure 4C, D). Thus, if a high-intensity light source is available, excitation at the edge of Aurora's action spectrum (595 nm, orange) is sufficient to block action potentials in pyramidal cells.

Compared to Aurora, and consistent with our measurements in HEK cells, Phobos showed a blue-shifted action spectrum, which peaked at 460 nm and was truncated in the long-wavelength light regime (Figure S5). The peak current was reduced to half-maximum between 500 and 525 nm (500 nm: 68.8 ± 5 % and 525 nm: 41 ± 5 %). Like Aurora, Phobos generated a fast inactivating current, which was absent when activated with more red-shifted light (Figure 4F). As for Aurora, the ability to block action potentials was tested with illumination at various wavelengths (365 to 635 nm) and intensities (0.1, 1, and 10 mW/mm^2) for 200 ms during 500 ms depolarization steps. In agreement with the measured action spectrum, spikes were efficiently blocked (>90 %) with light up to 525 nm at a saturating intensity of 10 mW/mm^2. At 1 mW/mm^2 spike block was only efficiently achieved between 435 to 500 nm. With 0.1 mW/mm^2 action potentials were not efficiently blocked anymore. The maximal effect (50 %) was reached at 460 nm, the peak of the action spectrum of Phobos (Figure 4G, H, S5).

Next we asked whether the bi-stable variants of Phobos, Aurora and iChloC (C128A) were suitable to block action potentials for an extended time period after a brief light flash and whether this block could be reverted with red-shifted illumination, as suggested by the HEK cell measurements. Like their parental constructs, Phobos^{CA}, Aurora^{CA} and iChloC^{CA} were fused with Citrine and expressed together with mCerulean. All three step-function aACRs produced photocurrents upon illumination in voltage clamp. Similar to HEK-cell

bioRxiv preprint doi: https://doi.org/10.1101/156422; this version posted June 27, 2017. The copyright holder for this preprint (which was not certified by peer review) is the author/funder. All rights reserved. No reuse allowed without permission.

measurements the net activation spectra were slightly blue-shifted compared to the parental fast cycling aACRs. Also, inactivation spectra peaked at similar wavelengths (Figures 5A-C, S6A-D). To assess spike-block performance, we injected repeated, depolarizing current steps (2 s duration) at an interval of 0.2 Hz in current clamp for one minute, which reliably evoked action potential firing (Figure 5D, S7). To open the respective step-function aACR and thereby inhibit action potentials, we applied a 20 ms light flash (Phobos^{CA}: 460 nm, iChloC^{CA}: 470 nm, Aurora^{CA}: 525 nm) after 5 s. Action potentials were efficiently blocked by Phobos^{CA} and iChloC^{CA} in the following 55 s (Figure S7). Also activation of Aurora^{CA} resulted in long-lasting inhibition of action potential firing. However, we noted a slight depolarization of the resting membrane potential in Aurora^{CA} expressing cells during current injection in the dark (Figure S7A). This might indicate a depolarizing leak conductance in Aurora^{CA} expressing neurons, which is further supported by altered membrane parameters and spike properties in the dark (Supplementary table 1). Moreover, the membrane markedly depolarized after light activation, which prevented complete spike block. These limitations have to be taken into account when considering Aurora^{CA} as a silencing tool in neurons.

In a subset of experiments, aACRs were closed with a second light flash (1 s, Phobos^{CA}: 595 nm, iChloC^{CA}: 635 nm, Aurora^{CA}: 660 nm) 30 s after the first light flash. Action potentials immediately returned to the same frequency as before the first light flash, indicating complete shut-down of the chloride conductance (Figure 5E-G). Since acceleration of channel closing depends on the light energy absorbed by the open channel, a longer illumination period at lower light intensities can be used if light power is limited (Figure S6E, F).

Light modulation of behavioral responses in *Drosophila*

To test if aACRs can functionally inhibit neurons *in vivo*, we used *Drosophila melanogaster* as a model organism. We tested whether the novel aACRs can functionally inhibit the larval nociceptive and motor systems. First, we compared the capacity of previously published enhanced halorhodopsin eNpHR [50] with iChloC [7] and Aurora to inhibit nociceptive class IV da (C4da) neurons, which mediate larval nocifensive rolling responses to mechanical stimulation [51]. All animals were raised in the presence of all-*trans* retinal (ATR). eNpHR expression in C4da neurons caused only unspecific defects in nociceptive responses and light-activation of eNpHR had no detectable further effect (Figure 6A). In contrast, iChloC activation by blue or green light significantly reduced mechano-nociceptive responses. Notably, 470 nm but not 525 nm illumination alone increased nociceptive responses in control animals that did not express light-activated channels, likely due to the innate blue light sensitivity of C4da neurons [16]. Activation of Aurora with 525 nm light strongly reduced nociceptive rolling, suggesting efficient silencing of C4da neurons at a wavelength that does not facilitate nociceptive responses (Figure 6A).

bioRxiv preprint doi: https://doi.org/10.1101/156422; this version posted June 27, 2017. The copyright holder for this preprint (which was not certified by peer review) is the author/funder. All rights reserved. No reuse allowed without permission.

We next compared the functionality of the newly generated aACRs in larval locomotion. We expressed aACRs in larval motor neurons and first analyzed their expression and localization. Aurora, Phobos and Phobos^{CA} were highly expressed in motor neurons and localized predominantly in the axon and at the neuromuscular junction (NMJ). All three aACRs co-localized with a cell surface marker suggesting efficient surface delivery (Figure S8). Importantly, NMJ morphology was not affected by aACR overexpression, indicating high tolerance in *Drosophila* neurons. We next assessed their efficiency in inhibiting locomotion upon light stimulation. Both, Phobos and Aurora-expressing animals that were raised in the presence of ATR slowed down significantly during a 15 s illumination period by 67.4 ± 2.6 % ($p < 0.0001$, n = 57 animals, repeated measures one-way ANOVA, followed by Sidak's multiple comparisons test) and 66.3 ± 1.8% ($p < 0.0001$, n = 52 animals, repeated measures one-way ANOVA, followed by Sidak's multiple comparisons test), respectively. After the light stimulus, the animals accelerated again, showing normal locomotion (Figure 6B-F). Due to the strong innate behavioral response to visible light [16], wild-type control animals also significantly reduced their velocity upon illumination (470 nm: 52.3 ± 4.5 %, $p < 0.0001$, n = 35; 525 nm 39.2 ± 4.5%, $p < 0.0001$, n = 34; Figure 6F, S9). However, this reduction was significantly smaller than in animals expressing Aurora or Phobos (Figure 6F & S9 A-C). Importantly, wild-type animals were not motionless during illumination. They rather displayed stereotypic head-turns, which signify the innate escape response and therefore reduced linear locomotion speed [52] (Videos 1&2). In contrast, activation of Phobos or Aurora also abolished head-turning and therefore efficiently inhibited the motor system (Videos 3&4).

Due to the direct impact of continuous illumination on locomotion, we reasoned that the step function mutations should allow us to uncouple the innate light response from the neuronal silencing effect. We found that Aurora^{CA} expression in larval motor neurons was toxic, perhaps due to leak currents in the dark. Phobos^{CA}, on the other hand, was well tolerated by larvae, and activation was able to fully inhibit larval locomotion, which was sustained after the light pulse ($p<0.0001$, n = 44 animals, repeated measures one-way ANOVA, followed by Sidak's multiple comparisons test, Figure 6G, H, Video 5). The open-state of Phobos^{CA} could be reverted with illumination at 595 nm resulting in efficient recovery of larval locomotion. In contrast, wild-type control animals only slowed down during the blue light pulse and immediately regained full locomotion speed after light shutoff (Figure S9D, E, Video 6). These results show that step-function aACRs can be used to modulate behavior in a binary manner.

Finally, to confirm that aACRs indeed have an inhibitory silencing effect on the motor system, we compared the effect of Phobos^{CA} activation on larval body length with that of Channelrhodopsin-2-XXL (ChR2^{XXL}) [35]. ChR2^{XXL} activation in motor neurons resulted in

bioRxiv preprint doi: https://doi.org/10.1101/156422; this version posted June 27, 2017. The copyright holder for this preprint (which was not certified by peer review) is the author/funder. All rights reserved. No reuse allowed without permission.

strong body wall muscle contraction and an effective shrinkage of the detectable larval body area, consistent with motor neuron activation (Figure 6 I, J). Conversely, Phobos^{CA} activation resulted in body wall muscle relaxation indicated byan increase in the detectable area due to lack of contracting segments. This data confirms the inhibitory nature of Phobos^{CA} action.

bioRxiv preprint doi: https://doi.org/10.1101/156422; this version posted June 27, 2017. The copyright holder for this preprint (which was not certified by peer review) is the author/funder. All rights reserved. No reuse allowed without permission.

Discussion:

We extensively explored the possibilities to engineer novel aACRs from 11 different well-characterized CCRs (Figure S1) by employing two independent strategies based on previous mutagenesis of *Cr*ChR2 [8] or the C1C2 chimera [6]. The latter strategy aimed at systematically replacing negative charges in the outer pore of the channel with positive or neutral charges, without compromising the photocycle or protein stability of C1C2. The second strategy was based on the exchange of an acidic glutamate for a basic arginine at position 90 (E90R) in the central gate of *Cr*ChR2. While both approaches led to increased anion selectivity, in both cases a significant portion of protons was still conducted by the engineered variants. In a second round of optimization, this residual proton conductance was eliminated by introducing additional mutations, yielding the two highly chloride selective aACRs iC++ and iChloC [5,7]. The successful conversion of two different, yet closely related CCRs (*Cr*ChR2 and C1C2, figure S10) prompted us to systematically investigate the applicability of the two conversion strategies to other CCRs. We focused mainly on CCRs with blue-, or red-shifted action spectra relative to iC++ and iChloC. We also asked if the iC++-strategy was applicable to *Cr*ChR2 and conversely, if the iChloC-strategy was applicable to C1C2. Interestingly, while ion selectivity could be inverted in *Cr*ChR2 with both strategies, conversion of C1C2 with the ChloC approach – albeit successful - yielded low channel expression in HEK cells and negligible photocurrents (Figure S2). Low expression or improper subcellular targeting was also observed for various CCRs converted with both strategies. Thus, both mutagenesis strategies were limited to a small subset of CCRs and not generalizable. The main limitation often appears to be the deleterious effect of mutagenesis on proper folding and plasma membrane localization of the channel. For example, both ChloC and iC++ conversion strategies failed for the three blue-shifted CCRs *Tc*ChR, *Ts*ChR, *Ps*ChR2 and the fast CCR Chronos due to loss of protein expression (except for the ChloC strategy on *Tc*ChR, which did not affect protein expression but failed to shift ion selectivity). Similarly, photocurrents of the mutated red-shifted CCRs *Vc*ChR1, C1V1b and Chrimson were extremely weak or absent altogether. However, in this case, despite resulting in poor expression and low photocurrents, the iC++ approach rendered *Vc*ChR1, C1V1b completely anion-selective.

The only CCR where both strategies yielded full anion selectivity without compromising photocurrents was *Co*ChR, which is closely related to C1C2 and *Cr*ChR2 (Figure S10). While the ChloC approach alone resulted in an incomplete shift of the ion selectivity, additional iChloC mutations rendered *Co*ChR completely anion-selective. However, as shown earlier, expression in neurons was cytotoxic, most likely due to leakage of the channel in the dark [7]. Since the ChloC/iChloC conversion strategy failed in all other CCRs, we assume that the disruption in the central gate caused by the mutation of glutamate to an arginine destabilized

bioRxiv preprint doi: https://doi.org/10.1101/156422; this version posted June 27, 2017. The copyright holder for this preprint (which was not certified by peer review) is the author/funder. All rights reserved. No reuse allowed without permission.

the protein. Alternatively, the hydrogen bonding network between amino acids in the central gate may be differently arranged in different CCRs.

Also the iC++ strategy was too disruptive in most cases and only yielded three new aACRs without introducing leakiness or compromising photocurrents. Of these three, two have a similar action spectrum than the original iC++ and only Aurora, which was derived from ReaChR, displayed an action spectrum that was red-shifted compared to existing aACRs. We mapped the CCRs which could be converted with both approaches on a phylogenetic tree. Interestingly, the conversion strategies were only successful in CCRs closely related to *Cr*ChR2 and C1C2 (Figure S10). A blue-shifted aACR could be generated by altering the action spectrum of an existing aACR. This was achieved by converting the two residues T159 and G163 of iC++ to G and A, respectively, similar to the blue/shifted CCRs *Tc*ChR, *Ts*ChR, *Ps*ChR2, yielding Phobos. In summary, we successfully produced both a red-shifted aACR by applying the iC++ strategy to ReaChR and a blue-shifted ACR by introducing two point mutations from blue-shifted CCRs in iC++.

The photocurrents produced by the natural *Gt*ACR1/2 are higher than those of any other ACR produced or discovered so far, probably due to their large unitary conductance. Therefore, nACRs may be favored over aACRs if acute, transient silencing is desired. However, nACRs may still generate significant photocurrents at the far edges of their absorption spectra, limiting their combination with other light-dependent applications. Moreover, step-function variants of nACRs that can be toggled between conducting and non-conducting states by light with different wavelengths have not been reported. Engineering true step-function opsins (SFO) [18,19] from nACRs is not straightforward due to the low degree of homology between nACRs and most CCRs/aACRs [53]. In contrast, the SFO-strategy was previously applied to iC++ where introduction of the C128A mutation yielded the SFO-aACR SwiChR++ [5]. In the present study, we demonstrate that Aurora, Phobos and the previously published iChloC can be turned into SFOs by the C128A mutation, slowing down channel closing by up to 4 orders of magnitude. All new aACRs harboring the C128A mutation could be completely closed with light red-shifted by approx. 110 – 170 nm compared to the activation light.

While iChloC^{CA} and Phobos^{CA} did not alter neuronal properties in the dark, Aurora^{CA} apparently was leaky in neurons, resulting in altered membrane properties in hippocampal neurons and developmental problems in *Drosophila*. Thus, despite successful transformation into an SFO-aACR, Aurora^{CA} cannot be recommended as an optogenetic tool due its side effects. No such problems were encountered with the original fast-closing version of Aurora. If long-wavelength activation is desired, iChloC^{CA} may be an alternative. The unexpected red-shift of iChloC^{CA} may be a direct consequence of the C128A and D156N mutations. Both

bioRxiv preprint doi: https://doi.org/10.1101/156422; this version posted June 27, 2017. The copyright holder for this preprint (which was not certified by peer review) is the author/funder. All rights reserved. No reuse allowed without permission.

residues are located inside the retinal binding pocket and interact with the retinal Schiff base. The thiol group of C128 was suggested to directly interact with the retinal molecule [47,54]. The altered hydrogen bonding network may lower the absorption energy required to switch the bound retinal from all-*trans* to 13-*cis*.

Optogenetic experiments involving behavioral read-out always carry the risk that the photoactivation light is directly sensed by the animal, potentially leading to wrong conclusions about the function of the neural circuit in question. Two strategies may be employed to avoid this experimental problem using SFO-aACRs. First, low-intensity light is integrated over time by SFO-aACRs, accumulating more and more channels in the open state. Compared to inhibition through light-driven ion pumps, where only a single ion is moved per absorbed photon, light-gated channels offer greater efficacy, and SFOs take this principle to the extreme. However, *Drosophila* larvae are detecting and avoiding even low-intensity light [55,56]. Interference with innate responses is avoided by uncoupling functional silencing from the light stimulus. This possibility is provided by the second important advantage of SFO-aACRs, which allows to temporally separate light activation of the anion channel from the behavioral read-out. All our new C128A mutants (iChloC^{CA}, Phobos^{CA} and Aurora^{CA}) are suitable to strongly attenuate action potential firing in neurons for at least 50 s after light shutoff (Figure S7C, D). This property enabled us to dissociate the silencing effects of the SFO-aACR from the light stimulus in *Drosophila* larvae. Activation of Phobos^{CA} with a brief light pulse stopped locomotion for an extended time period while wild-type larvae showed only a transient response (Figure S9D, E). In addition, locomotion could be restored by illumination with red light which does not affect natural behavior [55]. Thus, we provide proof-of-concept that defined neuronal populations in intact animals can be switched *off* and back *on* with brief light pulses, allowing investigation of behavioral effects without continuous illumination.

bioRxiv preprint doi: https://doi.org/10.1101/156422; this version posted June 27, 2017. The copyright holder for this preprint (which was not certified by peer review) is the author/funder. All rights reserved. No reuse allowed without permission.

Methods:

Molecular Biology and aACR variant design — Expression vectors encoding genes for ChRs where constructed using conventional PCR and restriction enzyme-based cloning methods (FastDigest, Thermo Fisher Scientific, Waltham, MA). Briefly, ChR cDNAs were cloned into p-EGFP-C1 vectors using NheI and AgeI restriction sites. EGFP was replaced by mCherry using AgeI and XhoI restriction sites except for iChloC variants where a p-EGFP-N1 vector was used. The QuickChange II kit (Agilent Technologies, Santa Clara, CA) was used to exchange single or multiple amino acids (C128A, T159G and G163A) in ChloC/iChloC based variants. For the iC++ based approach, ChR variants with the replaced N-terminus of iC++ and all iC++ homologous mutations were constructed *in-silico*, synthesized (GenScript, NJ) and cloned into p-EGFP-C1 vectors as described above. Amino acid sequences and mutations can be found in the supplementary material (Figure S1). We deposited the plasmids encoding for aACRs with the Addgene plasmid repository (#98165: p-mCherry-C1-iC++, #98166: p-mCherry-C1-Phobos, #98167: p-mCherry-C1-Aurora, #98168: p-mCherry-C1-iC++_CA, #98169: p-mCherry-C1-Phobos_CA, #98170: p-mCherry-C1-Aurora_CA, # 98171: p-mCherry-N1-iChloC_CA, #98172: p-mCherry-C1-iChR2++, #98173: p-mCherry-C1-iCoChR++).

HEK293 cell culture — HEK-293 cells (ACC-305, catalogue no. 85120602, Sigma-Aldrich, Munich, Germany) were cultured at 5 % CO_2 and 37 °C in Dulbecco's minimal essential medium (DMEM) supplemented with 10 % fetal bovine serum (FBS) and 100 µg/ml penicillin/streptomycin (all from Biochrom, Berlin, Germany). Cells where routinely tested with DAPI staining and PCR assay for mycoplasma contamination. For electrical recordings, cells were seeded onto poly-lysine coated glass coverslips at a concentration of 0.5×10^5 cells*ml^{-1} (2 ml total in 35 mm standard cell culture dishes) and supplemented with a final concentration of 1 µM all-*trans* retinal (Sigma-Aldrich, Munich, Germany). For confocal imaging cells were seeded with the same protocol in poly-lysine coated 35 mm glass bottom dishes (MaTek, Ashland, MA). Cells were transfected with aACR-cDNA using Fugene HD (Roche, Mannheim, Germany) 36 h before measurements.

Electrophysiological recordings in HEK293 cells — aACR expressing HEK cells where patched at low chloride conditions (10 mM intra- and extracellular). In whole-cell configuration the extracellular buffer was changed to high chloride (150 mM), resulting in a liquid junction potential of 10.5 mV that was corrected on-line. The buffer composition for the pipette solution (10 mM Cl^-) was (in mM): 2 $MgCl_2$, 2 $CaCl_2$, 1 KCl, 1 CsCl, 10 EGTA, 10 HEPES, 110 Na-Aspartate. The low/high chloride bath solution (10/150 mM Cl^-) was composed of (in mM): 2 $MgCl_2$, 2 CaCl2, 1 KCl, 1 CsCl, 10 HEPES, 0/140 NaCl, 140/0 Na-Aspartate. All buffers were adjusted with N-methyl-D-glucamine to pH 7.2. The final

bioRxiv preprint doi: https://doi.org/10.1101/156422; this version posted June 27, 2017. The copyright holder for this preprint (which was not certified by peer review) is the author/funder. All rights reserved. No reuse allowed without permission.

osmolarity was adjusted to 320 mOsm for extracellular solutions and 290 mOsm for intracellular solutions. External buffer solutions were exchanged by perfusion of at least 2.5 ml of the respective buffer into the custom made recording chamber (volume ~500 µl) while the bath level was kept constant with a ringer bath handler (MCPU, Lorenz Messgerätebau, Katlenburg-Lindau, Germany). Patch pipettes were pulled using a P1000 micropipette puller (Sutter Instruments, Novato, CA), and fire-polished. Pipette resistance was 1.5 to 2.5 MΩ. A 140 mM NaCl agar bridge served as reference (bath) electrode. In whole-cell recordings membrane resistance was >500 MΩ (typically >1 GΩ) and access resistance was below 10 MΩ. All experiments were carried out at 25 °C. Signals were amplified (AxoPatch200B), digitized (DigiData1400) and acquired using Clampex 10.4 Software (all from Molecular Devices, Sunnyvale, CA). Holding potentials were varied between -80 and +40 mV as indicated. A detailed protocol can be found in Grimm et. al [24].

A Polychrome V light source (TILL Photonics, Planegg, Germany) was used in most HEK-cell experiments. The half band width was set to ±7 nm for all measurements. Actinic light was coupled into an Axiovert 100 microscope (Carl Zeiss, Jena, Germany) and delivered to the sample using a 90/10 beamsplitter (Chroma, Bellows Falls, VT). Light exposure was controlled with a programmable shutter system (VS25 and VCM-D1, Vincent Associates, Rochester, NY). Intensities were measured in the sample plane with a calibrated optometer (P9710, Gigahertz Optik, Türkenfeld, Germany). Light intensities were calculated for the illuminated field of the W Plan-Apochromat 40x/1.0 DIC objective (0.066 mm², Carl Zeiss).

To record action spectra, a motorized neutral density filter wheel (NDF) (Newport, Irvine, CA) was inserted into the light path between the Polychrome V and the microscope to obtain the same photon irradiance for all wavelengths (390 to 670 nm; 10 or 20 nm steps). Custom software written in LabVIEW (National Instruments, Austin, TX) was used for control and synchronization with electrophysiological experiments. Light was applied for 10 ms at 0 mV holding potential. Minimal deviations in photon irradiance were corrected by linear normalization post measurements.

To record inactivation spectra of step-function aACRs, a 150 W Xenon lamp (LOT-QuantumDesign, Darmstad, Germany), filtered with single bandpass filters (460±10 nm, 490±8 nm and 520±20 nm) was coupled into the light path using a 30/70 beamsplitter (Chroma, Bellows Falls, VT) to activate slow-cycling aACRs. The 10 ms light exposure was controlled with the same programmable shutter system as used for the Polychrome V. Next, light of various wavelengths at the same photon irradiance (adjusted as described above) was applied for 8 s to inactivate (or additionally activate) aACRs, followed by complete channel closing achieved by application of red light for another 8 s. The holding potential was kept at 0 mV.

bioRxiv preprint doi: https://doi.org/10.1101/156422; this version posted June 27, 2017. The copyright holder for this preprint (which was not certified by peer review) is the author/funder. All rights reserved. No reuse allowed without permission.

For light titration experiments, ND filters (SCHOTT, Mainz, Germany) were used for attenuation. Activating light was applied for 12 s. The holding potential was kept at 20 mV. In case of step-function aACRs, channel closing was accelerated with application of red light between single trials.

Analysis of HEK293 cell electrophysiology — Data were analyzed using Clampfit 10.4 (Molecular Devices, Sunnyvale, CA) and Origin 9 (OriginLab, Northampton, MA). Stationary photocurrents were measured for the last 40 ms of illumination period or for 40 ms, 2 s after activation of step-function variants. To obtain reversal potentials (E_{rev}), photocurrents were plotted against the respective holding potential. Next, E_{rev} was calculated from the intersection of the current-voltage relation with the voltage axis. For action spectra, photocurrents were normalized to the maximum. To determine inactivation spectra (Figure 2E), mean stationary currents before and after additional activation/inactivation light (1 s after light was switched off) were averaged over a 200 ms period. The current difference (before-after) was divided by the current prior to inactivation (Figure 2D) and plotted against the wavelengths. Additional activation was normalized to maximum, whereas inactivation was not further normalized. The maximum response wavelength (λ_{max}) was determined by fitting single recorded action spectra with a 3-parameter Weibull function. Half maximal effective light dose values (EC_{50}) were determined by fitting single light titration curves by logistic growth function. Kinetic properties were determined by mono- or double-exponential fits and apparent closing constants were reported. For representative closing kinetic traces (Figure 2A), signals were binned to 50 points per decade with a custom written Matlab script (The MathWorks, Natick, MA). All data are given as mean ± standard error of the mean (SEM).

Epifluorescence and bright-field microscopy — Fluorescence HEK-cell images shown in figures S2 and S3 were acquired with a triple band ECFP/EYFP/mCherry 69008 filterset (Chroma, Bellows Falls, VT, USA) and a Wat-221S CCD camera (Watec, Tsuruoka, Japan) on the same Axiovert 100 microscope (Carl Zeiss) setup used for electrophysiological recordings (see above). Fluorescence excitation of mCherry was performed using Polychrome V set to 590±15 nm. Background-subtracted images were calculated with Fijij [25].

Confocal microscopy — Confocal HEK-cell images shown in figure 3 were taken with a FV1000 confocal laser scanning microscope equipped with an UPLSAPO 60XW objective (Olympus, Hamburg, Germany). The membrane of cells expressing aACR variants fused to mCherry was labeled with Vybrant DiO (ThermoFisher Scientific). mCherry was excited with a 559 nm diode laser and DiO was excited with a 488 nm Argon laser. Mean fluorescence intensities (per area) of the respective aACR-mCherry fusion construct either in the cell membrane (identified by DiO) or within the cell were evaluated (mean background fluorescence was subtracted) for three equatorial slices per cell using a custom Fiji macro

bioRxiv preprint doi: https://doi.org/10.1101/156422; this version posted June 27, 2017. The copyright holder for this preprint (which was not certified by peer review) is the author/funder. All rights reserved. No reuse allowed without permission.

553 and then averaged. The relative membrane targeting values were determined by dividing
554 mean fluorescence density in the cell membrane by the sum of the fluorescence densities
555 (membrane and cytosol).

556 *Two-photon microscopy* – Neurons in organotypic slice cultures were imaged with two-
557 photon microscopy (980 nm excitation) to characterize dendritic morphology and the
558 subcellular localization of citrine-labeled aACRs. The custom-built microscope was controlled
559 by ScanImage software (HHMI Janelia Farm) [26]. Green fluorescence was detected through
560 the objective (LUMPLFLN 60XW, Olympus, Hamburg, Germany) and the oil-immersion
561 condenser (1.4 NA) using GaAsP-PMTs (Hamamatsu, Japan).

562 *Neuronal recordings in hippocampal slice cultures* – All aACR mutants were subcloned into
563 identical neuron-specific expression vectors (pAAV backbone, human *synapsin* promoter),
564 followed by the sequence for a citrine fluorescent protein [27]. We deposited the AAV-plasmids
565 encoding aACRs with the Addgene plasmid repository (#98216: Phobos-Citrine, #98217,
566 Aurora-Citrine, #98218: Phobos^{CA}-Citrine, #98219: Aurora^{CA}-Citrine, # 98220: iChloC^{CA}-
567 Citrine). Organotypic slice cultures of rat hippocampus were prepared as described [28] and
568 transfected by single-cell electroporation [29] after 14 days *in vitro* (DIV). Plasmids were each
569 diluted to 20 ng/µl in K-gluconate–based solution consisting of (in mM): 135 K-gluconate,
570 4 $MgCl_2$, 4 Na_2-ATP, 0.4 Na-GTP, 10 Na_2-phosphocreatine, 3 ascorbate, 0.02 Alexa Fluor
571 594, and 10 HEPES (pH 7.2). An Axoporator 800A (Molecular Devices) was used to deliver
572 50 hyperpolarizing pulses (−12 mV, 0.5 ms) at 50 Hz. At DIV 18-20, targeted patch-clamp
573 recordings of transfected neurons were performed under visual guidance using a BX-51WI
574 microscope (Olympus), a Multiclamp 700B amplifier (Molecular Devices), and Ephus
575 software (HHMI Janelia Farm) [30]. Patch pipettes with a tip resistance of 3-4 MΩ were filled
576 with (in mM): 135 K-gluconate, 4 $MgCl_2$, 4 Na_2-ATP, 0.4 Na-GTP, 10 Na_2-phosphocreatine,
577 3 ascorbate, 0.2 EGTA, and 10 HEPES (pH 7.2). Artificial cerebrospinal fluid (ACSF)
578 consisted of (in mM): 135 NaCl, 2.5 KCl, 2 $CaCl_2$, 1 $MgCl_2$, 10 Na-HEPES, 12.5 D-glucose,
579 1.25 NaH_2PO_4 (pH 7.4). Synaptic currents were blocked with 10 µM CPPene, 10 µM NBQX,
580 and 10 µM bicuculline or 100 µm picrotoxin (Tocris, Bristol, UK). Measurements were
581 corrected for a liquid junction potential of -10.6 mV. A 16-channel pE-4000 LED light engine
582 (CoolLED, Andover, UK) was used for epifluorescence excitation and delivery of light pulses
583 (ranging from 365 to 660 nm). Light intensity was measured in the object plane with a
584 1918-R power meter equipped with a calibrated 818-ST2-UV/D detector (Newport, Irvine CA)
585 and divided by the illuminated field (0.134 mm^2) of the LUMPLFLN 60XW objective
586 (Olympus).

587 *Behavioral assays in Drosophila melanogaster* – cDNAs encoding aACR were codon-
588 optimized for *Drosophila melanogaster*, synthesized (Thermo Fisher Scientific) and cloned

bioRxiv preprint doi: https://doi.org/10.1101/156422; this version posted June 27, 2017. The copyright holder for this preprint (which was not certified by peer review) is the author/funder. All rights reserved. No reuse allowed without permission.

into a 20x UAS vector (pJFRC7, Addgene #26220) [31] together with a C-terminal mCerulean3 [32] for Aurora, Phobos, and Phobos^{CA}, or tdTomato [33] for iChloC. Transgenic lines were generated in the attP2 locus using phiC31-mediated transgenesis [34]. The following additional lines were used: *UAS-ChR-XXL* [35], *UAS-eNpHR3.0-YFP, ppk-Gal4* [36] for C4da and *vglut^{ok371}-Gal4* [37] for motor neuron expression of aACRs.

Embryos from experimental crosses were collected on grape juice agar plates and supplied with fresh yeast paste containing 5 mM all-*trans* retinal (ATR) and kept at 25 °C in the dark. Staged and density controlled 3rd instar larvae (96 h ± 3 h after egg laying) were collected under low red light illumination (>700 nm).

For mechano-nociception, animals were placed on a 2 % agar plate and forward-locomoting larvae were stimulated on mid-abdominal segments (3 - 5) with a 50 mN *von Frey* filament twice within 2 s. The behavioral response was visually scored under a stereoscope as non-nociceptive (no response, stop, stop and turn) or nociceptive (bending, rolling). For analysis, only nocifensive rolling behavior (full 360° turn along the body axis) was compared. For simultaneous aACR activation, ATR-fed staged and density-controlled 3rd instar larvae (96±3 h after egg laying (AEL)) were exposed to 470 nm (0.2 mW/mm²) or 525 nm (0.57 mW/mm²) light from a mercury vapor short arc light source under a stereoscope (Olympus SZX16 with X-Cite 120Q illumination system, Excelitas Technologies, Waltham, MA). Each genotype was tested multiple times on different days and data from all trials was combined. Statistical significance was calculated using a chi^2 test.

Larval locomotion analysis was performed using a frustrated total internal reflection (FTIR) based tracking system (FIM, University of Münster) [38]. Five freely moving larvae per trial were placed on a 1 % agar plate and video-captured with a CMOS camera (ac2040-25gm, Basler, Ahrensburg, Germany). During free locomotion, aACRs were activated by illumination with 525 nm light from a RGB-BL-S-Q-1R LED backlight (Phlox, Aix-en-Provence, France) or 460, 470 and 595 nm light from a pE-4000 (CoolLED) coupled to a light guide with custom collimator lenses. Animal locomotion was tracked with 10 frames/s for up to 90 s and then analyzed using FIMtracking software (FIM, University of Münster). Each genotype was tested multiple times on different days and data from all trials were combined. For analysis, only animals displaying continuous locomotion before the light stimulus were kept. Locomotion velocity was analyzed over time. For comparison, velocities were averaged over a 5 s interval, each before, during and after light mediated activation of aACRs.

To compare the effect on body wall muscle contraction of inhibitory aACRs with excitatory ChR2^{XXL} [35] we analyzed the larval area change before and after light activation using FIMtracking software (FIM, University of Münster). Animal size was averaged over a 5 s

bioRxiv preprint doi: https://doi.org/10.1101/156422; this version posted June 27, 2017. The copyright holder for this preprint (which was not certified by peer review) is the author/funder. All rights reserved. No reuse allowed without permission.

interval before and after light activation for analysis. Statistical significance was calculated by ANOVA followed by a Sidak's multiple comparisons test for repeated measurements or a (non-parametric) Kruskal-Wallis test followed by a Dunn's multiple comparisons test for comparisons between groups.

Immunohistochemistry of larval neuromuscular junctions (NMJs). – 3rd instar larval fillets were dissected in PBS and pinned down on Sylgard plates (Dow Corning, Midland, MI) with minutien pins (Fine Science Tools, Heidelberg, Germany). Animals were cut open dorsally and internal organs were removed while leaving the nervous system intact. Fillet preparations were fixed in 4 % formaldehyde/PBS for 20 min, blocked in PBS/0.3 % Triton X-100 containing 5 % normal donkey serum (Jackson ImmunoResearch Laboratories, West Grove, PA). Larvae expressing Aurora–Cerulean or Phobos^{CA}–Cerulean in motor neurons (*ok371-Gal4*) were immunostained using a rabbit anti-GFP antibody (1:500, cat. no. A-11122, 1DB-ID: 1DB-001-0000868907, ThermoFisher Scientific). Secondary donkey anti-rabbit-DyLight488 and anti-HRP-Cy3 antibodies were used at 1:300 dilution (cat. no.123-165-021, DB-ID:1DB-001-0000865678, Jackson ImmunoResearch). NMJs at muscle 6/7 were visualized by confocal microscopy with a 20x/NA 0.8 air objective (Zeiss LSM700, Carl Zeiss).

Statistics – All statistical analyses were performed using GraphPad Prism 6.0 or Origin 10.5. Data were tested for normal distribution by D'Agostino & Pearson omnibus normality test. Normally distributed data were tested for significant differences (*P<0.05, **P<0.01, ***P<0.001 and ****P<0.0001) with one-way repeated-measures analysis of variance followed by Tukey's, Dunnett's or Sidak's multiple comparisons test. Not normally distributed data were tested with the nonparametric Kruskal-Wallis test followed by Dunn's multiple comparisons test. Data are presented as mean ± standard error of the mean (SEM). No statistical measures were used to estimate sample size since effect size was unknown. Given n numbers represent biological replicates (i.e. HEK-cells, neurons, *Drosophila* larvae). For HEK-cell measurements and hippocampal neuronal recordings investigators were not blinded to the group allocation during the experiments. Nociceptive *Drosophila* experiments were blinded. Data analysis was done by expert investigators who did not carry out the experiments. In addition, unsupervised analysis software was used if possible to preclude investigator biases. All experiments were done with interleaved controls and treatment groups were mixed, where possible.

Data availability – The authors declare that all data and code supporting the findings of this study are included in the manuscript and its Supplementary Information or are available from the corresponding authors on request. The plasmids used in this study are deposited with the Addgene plasmid repository.

bioRxiv preprint doi: https://doi.org/10.1101/156422; this version posted June 27, 2017. The copyright holder for this preprint (which was not certified by peer review) is the author/funder. All rights reserved. No reuse allowed without permission.

References

1 Govorunova, E. G., Sineshchekov, O. A. & Spudich, J. L. Proteomonas sulcata ACR1: A Fast Anion Channelrhodopsin. *Photochemistry and photobiology*, doi:10.1111/php.12558 (2015).

2 Govorunova, E. G., Sineshchekov, O. A., Janz, R., Liu, X. & Spudich, J. L. NEUROSCIENCE. Natural light-gated anion channels: A family of microbial rhodopsins for advanced optogenetics. *Science* **349**, 647-650, doi:10.1126/science.aaa7484 (2015).

3 Wietek, J., Broser, M., Krause, B. S. & Hegemann, P. Identification of a Natural Green Light Absorbing Chloride Conducting Channelrhodopsin from Proteomonas sulcata. *J Biol Chem* **291**, 4121-4127, doi:10.1074/jbc.M115.699637 (2016).

4 Govorunova, E. G. *et al.* The Expanding Family of Natural Anion Channelrhodopsins Reveals Large Variations in Kinetics, Conductance, and Spectral Sensitivity. *Scientific reports* **7**, 43358, doi:10.1038/srep43358 (2017).

5 Berndt, A. *et al.* Structural foundations of optogenetics: Determinants of channelrhodopsin ion selectivity. *Proc Natl Acad Sci U S A* **113**, 822-829, doi:10.1073/pnas.1523341113 (2016).

6 Berndt, A., Lee, S. Y., Ramakrishnan, C. & Deisseroth, K. Structure-guided transformation of channelrhodopsin into a light-activated chloride channel. *Science* **344**, 420-424, doi:10.1126/science.1252367 (2014).

7 Wietek, J. *et al.* An improved chloride-conducting channelrhodopsin for light-induced inhibition of neuronal activity in vivo. *Scientific reports* **5**, 14807, doi:10.1038/srep14807 (2015).

8 Wietek, J. *et al.* Conversion of channelrhodopsin into a light-gated chloride channel. *Science* **344**, 409-412, doi:10.1126/science.1249375 (2014).

9 Takahashi, N., Oertner, T. G., Hegemann, P. & Larkum, M. E. Active cortical dendrites modulate perception. *Science* **354**, 1587-1590, doi:10.1126/science.aah6066 (2016).

10 Kim, H., Ahrlund-Richter, S., Wang, X., Deisseroth, K. & Carlen, M. Prefrontal Parvalbumin Neurons in Control of Attention. *Cell* **164**, 208-218, doi:10.1016/j.cell.2015.11.038 (2016).

11 Park, S. *et al.* Neuronal Allocation to a Hippocampal Engram. *Neuropsychopharmacology* **41**, 2987-2993, doi:10.1038/npp.2016.73 (2016).

12 Chung, S. *et al.* Identification of preoptic sleep neurons using retrograde labelling and gene profiling. *Nature* **545**, 477-481, doi:10.1038/nature22350 (2017).

13 Al-Juboori, S. I. *et al.* Light scattering properties vary across different regions of the adult mouse brain. *PLoS One* **8**, e67626, doi:10.1371/journal.pone.0067626 (2013).

14 Yona, G., Meitav, N., Kahn, I. & Shoham, S. Realistic Numerical and Analytical Modeling of Light Scattering in Brain Tissue for Optogenetic Applications(1,2,3). *eNeuro* **3**, doi:10.1523/ENEURO.0059-15.2015 (2016).

15 Stujenske, J. M., Spellman, T. & Gordon, J. A. Modeling the Spatiotemporal Dynamics of Light and Heat Propagation for In Vivo Optogenetics. *Cell reports* **12**, 525-534, doi:10.1016/j.celrep.2015.06.036 (2015).

bioRxiv preprint doi: https://doi.org/10.1101/156422; this version posted June 27, 2017. The copyright holder for this preprint (which was not certified by peer review) is the author/funder. All rights reserved. No reuse allowed without permission.

16 Xiang, Y. *et al.* Light-avoidance-mediating photoreceptors tile the Drosophila larval body wall. *Nature* **468**, 921-926, doi:10.1038/nature09576 (2010).

17 Ward, A., Liu, J., Feng, Z. & Xu, X. Z. Light-sensitive neurons and channels mediate phototaxis in C. elegans. *Nat Neurosci* **11**, 916-922, doi:10.1038/nn.2155 (2008).

18 Berndt, A., Yizhar, O., Gunaydin, L. A., Hegemann, P. & Deisseroth, K. Bi-stable neural state switches. *Nat Neurosci* **12**, 229-234, doi:10.1038/nn.2247 (2009).

19 Yizhar, O. *et al.* Neocortical excitation/inhibition balance in information processing and social dysfunction. *Nature* **477**, 171-178, doi:10.1038/nature10360 (2011).

20 Han, X. & Boyden, E. S. Multiple-color optical activation, silencing, and desynchronization of neural activity, with single-spike temporal resolution. *PLoS One* **2**, e299, doi:10.1371/journal.pone.0000299 (2007).

21 Zhang, F., Aravanis, A. M., Adamantidis, A., de Lecea, L. & Deisseroth, K. Circuit-breakers: optical technologies for probing neural signals and systems. *Nat Rev Neurosci* **8**, 577-581, doi:10.1038/nrn2192 (2007).

22 Chow, B. Y. *et al.* High-performance genetically targetable optical neural silencing by light-driven proton pumps. *Nature* **463**, 98-102, doi:10.1038/nature08652 (2010).

23 Jan, Y. N. & Jan, L. Y. Branching out: mechanisms of dendritic arborization. *Nat Rev Neurosci* **11**, 316-328, doi:10.1038/nrn2836 (2010).

24 Grimm, C., Vierock, J., Hegemann, P. & Wietek, J. Whole-cell Patch-clamp Recordings for Electrophysiological Determination of Ion Selectivity in Channelrhodopsins. *J Vis Exp*, e55497, doi:10.3791/55497 (2017).

25 Schindelin, J. *et al.* Fiji: an open-source platform for biological-image analysis. *Nat Methods* **9**, 676-682, doi:10.1038/nmeth.2019 (2012).

26 Pologruto, T. A., Sabatini, B. L. & Svoboda, K. ScanImage: flexible software for operating laser scanning microscopes. *Biomed Eng Online* **2**, 13, doi:10.1186/1475-925X-2-13 (2003).

27 Griesbeck, O., Baird, G. S., Campbell, R. E., Zacharias, D. A. & Tsien, R. Y. Reducing the environmental sensitivity of yellow fluorescent protein. Mechanism and applications. *The Journal of biological chemistry* **276**, 29188-29194, doi:10.1074/jbc.M102815200 (2001).

28 Gee, C. E., Ohmert, I., Wiegert, J. S. & Oertner, T. G. Preparation of Slice Cultures from Rodent Hippocampus. *Cold Spring Harbor protocols* **2017**, pdb prot094888, doi:10.1101/pdb.prot094888 (2017).

29 Wiegert, J. S., Gee, C. E. & Oertner, T. G. Single-Cell Electroporation of Neurons. *Cold Spring Harbor protocols* **2017**, pdb prot094904, doi:10.1101/pdb.prot094904 (2017).

30 Suter, B. A. *et al.* Ephus: multipurpose data acquisition software for neuroscience experiments. *Front Neural Circuits* **4**, 100, doi:10.3389/fncir.2010.00100 (2010).

31 Pfeiffer, B. D. *et al.* Refinement of tools for targeted gene expression in Drosophila. *Genetics* **186**, 735-755, doi:10.1534/genetics.110.119917 (2010).

32 Markwardt, M. L. *et al.* An improved cerulean fluorescent protein with enhanced brightness and reduced reversible photoswitching. *PLoS One* **6**, e17896, doi:10.1371/journal.pone.0017896 (2011).

bioRxiv preprint doi: https://doi.org/10.1101/156422; this version posted June 27, 2017. The copyright holder for this preprint (which was not certified by peer review) is the author/funder. All rights reserved. No reuse allowed without permission.

33 Shaner, N. C. *et al.* Improving the photostability of bright monomeric orange and red fluorescent proteins. *Nat Methods* **5**, 545-551, doi:10.1038/nmeth.1209 (2008).

34 Groth, A. C., Fish, M., Nusse, R. & Calos, M. P. Construction of transgenic Drosophila by using the site-specific integrase from phage phiC31. *Genetics* **166**, 1775-1782 (2004).

35 Dawydow, A. *et al.* Channelrhodopsin-2-XXL, a powerful optogenetic tool for low-light applications. *Proceedings of the National Academy of Sciences of the United States of America* **111**, 13972-13977, doi:10.1073/pnas.1408269111 (2014).

36 Han, C., Jan, L. Y. & Jan, Y. N. Enhancer-driven membrane markers for analysis of nonautonomous mechanisms reveal neuron-glia interactions in Drosophila. *Proceedings of the National Academy of Sciences of the United States of America* **108**, 9673-9678, doi:10.1073/pnas.1106386108 (2011).

37 Mahr, A. & Aberle, H. The expression pattern of the Drosophila vesicular glutamate transporter: a marker protein for motoneurons and glutamatergic centers in the brain. *Gene Expr Patterns* **6**, 299-309, doi:10.1016/j.modgep.2005.07.006 (2006).

38 Risse, B. *et al.* FIM, a novel FTIR-based imaging method for high throughput locomotion analysis. *PLoS One* **8**, e53963, doi:10.1371/journal.pone.0053963 (2013).

39 Klapoetke, N. C. *et al.* Independent optical excitation of distinct neural populations. *Nat Methods* **11**, 338-346, doi:10.1038/nmeth.2836 (2014).

40 Govorunova, E. G., Sineshchekov, O. A., Li, H., Janz, R. & Spudich, J. L. Characterization of a highly efficient blue-shifted channelrhodopsin from the marine alga Platymonas subcordiformis. *The Journal of biological chemistry* **288**, 29911-29922, doi:10.1074/jbc.M113.505495 (2013).

41 Zhang, F. *et al.* Red-shifted optogenetic excitation: a tool for fast neural control derived from Volvox carteri. *Nat Neurosci* **11**, 631-633, doi:10.1038/nn.2120 (2008).

42 Wang, H. *et al.* Molecular determinants differentiating photocurrent properties of two channelrhodopsins from chlamydomonas. *The Journal of biological chemistry* **284**, 5685-5696, doi:10.1074/jbc.M807632200 (2009).

43 Tsunoda, S. P. & Hegemann, P. Glu 87 of channelrhodopsin-1 causes pH-dependent color tuning and fast photocurrent inactivation. *Photochemistry and photobiology* **85**, 564-569, doi:10.1111/j.1751-1097.2008.00519.x (2009).

44 Prigge, M. *et al.* Color-tuned channelrhodopsins for multiwavelength optogenetics. *The Journal of biological chemistry* **287**, 31804-31812, doi:10.1074/jbc.M112.391185 (2012).

45 Yizhar, O., Fenno, L. E., Davidson, T. J., Mogri, M. & Deisseroth, K. Optogenetics in neural systems. *Neuron* **71**, 9-34, doi:10.1016/j.neuron.2011.06.004 (2011).

46 Lin, J. Y., Knutsen, P. M., Muller, A., Kleinfeld, D. & Tsien, R. Y. ReaChR: a red-shifted variant of channelrhodopsin enables deep transcranial optogenetic excitation. *Nat Neurosci* **16**, 1499-1508, doi:10.1038/nn.3502 (2013).

47 Kato, H. E. *et al.* Structural basis for Na(+) transport mechanism by a light-driven Na(+) pump. *Nature* **521**, 48-53, doi:10.1038/nature14322 (2015).

48 Krause, B. S. *et al.* Complex Photochemistry within the Green-Absorbing Channelrhodopsin ReaChR. *Biophys J* **112**, 1166-1175, doi:10.1016/j.bpj.2017.02.001 (2017).

bioRxiv preprint doi: https://doi.org/10.1101/156422; this version posted June 27, 2017. The copyright holder for this preprint (which was not certified by peer review) is the author/funder. All rights reserved. No reuse allowed without permission.

49 Hososhima, S., Sakai, S., Ishizuka, T. & Yawo, H. Kinetic evaluation of photosensitivity in bi-stable variants of chimeric channelrhodopsins. *PLoS One* **10**, e0119558, doi:10.1371/journal.pone.0119558 (2015).

50 Gradinaru, V., Thompson, K. R. & Deisseroth, K. eNpHR: a Natronomonas halorhodopsin enhanced for optogenetic applications. *Brain Cell Biol* **36**, 129-139, doi:10.1007/s11068-008-9027-6 (2008).

51 Hwang, R. Y. *et al.* Nociceptive neurons protect Drosophila larvae from parasitoid wasps. *Curr Biol* **17**, 2105-2116, doi:10.1016/j.cub.2007.11.029 (2007).

52 Kane, E. A. *et al.* Sensorimotor structure of Drosophila larva phototaxis. *Proceedings of the National Academy of Sciences of the United States of America* **110**, E3868-3877, doi:10.1073/pnas.1215295110 (2013).

53 Sineshchekov, O. A., Govorunova, E. G., Li, H. & Spudich, J. L. Gating mechanisms of a natural anion channelrhodopsin. *Proceedings of the National Academy of Sciences of the United States of America* **112**, 14236-14241, doi:10.1073/pnas.1513602112 (2015).

54 Guo, Y. *et al.* Active site structure and absorption spectrum of channelrhodopsin-2 wild-type and C128T mutant. *Chemical Science* **7**, 3879-3891, doi:10.1039/c6sc00468g (2016).

55 Keene, A. C. & Sprecher, S. G. Seeing the light: photobehavior in fruit fly larvae. *Trends Neurosci* **35**, 104-110, doi:10.1016/j.tins.2011.11.003 (2012).

56 Busto, M., Iyengar, B. & Campos, A. R. Genetic dissection of behavior: modulation of locomotion by light in the Drosophila melanogaster larva requires genetically distinct visual system functions. *J Neurosci* **19**, 3337-3344 (1999).

bioRxiv preprint doi: https://doi.org/10.1101/156422; this version posted June 27, 2017. The copyright holder for this preprint (which was not certified by peer review) is the author/funder. All rights reserved. No reuse allowed without permission.

Acknowledgements:

We thank Edward Boyden (*Tc*ChR, *Ts*ChR, *Co*ChR, Chronos and Chrimson), Johannes Vierock (C1C2) and the late Roger Y. Tsien (ReaChR) for providing plasmids encoding for CCRs. We further thank Ivan Haralampiev, Thomas Korte and Andreas Hermann for help with confocal microscopy, Iris Ohmert and Sabine Graf for hippocampal slice cultures, Benjamin S. Krause for discussions and Kathrin Sauter, Maila Reh, Altina Klein and Tharsana Tharmalingam for technical assistance.

This work was funded by grants from the European Research Council (ERC-2016-StG 714762 to J.S.W), the German Research Foundation (SPP 1926 to P.S. & J.S.W.; FOR 2419 to J.S.W. and T.G.O., SFB1078 B2, FOR 1279, SPP 1665 to P.H. and T.G.O.). P.H. is Hertie Senior Professor for Neuroscience and supported by the Hertie Foundation.

Author contributions:

J.W., T.G.O., P.S., P.H. and J.S.W. conceived the study and planned experiments, J.W., S.R.R., J.T., F.T., C.G. and J.S.W. performed the experiments, J.W., S.R.R., J.T., F.T., C.G., P.S. and J.S.W. analyzed the data. J.W. and J.S.W. wrote the manuscript with contributions from all authors.

Competing interests:

The authors declare no competing financial interests.

bioRxiv preprint doi: https://doi.org/10.1101/156422; this version posted June 27, 2017. The copyright holder for this preprint (which was not certified by peer review) is the author/funder. All rights reserved. No reuse allowed without permission.

Figure legends:

Figure 1: Construct design and screening result for aACRs. (**A**) Conversion strategies yielding the aACRs ChloC, iChloC (left) and iC++ (right). The transmembrane helices of *Cr*ChR2 (ChR2) and *Cr*ChR1 (ChR1) are shown in green and purple, respectively. The positions of the outer access channel, central gate (including retinal binding pocket) and inner gate are indicated by gray horizontal stripes. Mutations are displayed as circles at the relative position within the respective helix. ChloC has the mutations E90R and T159C, whereas in iChloC E83Q and E101S were additionally introduced. The D156N mutation from slowChloC is also present in iChloC (left). iC++ exhibits 10 mutations and a modified N-terminal sequence (right). (**B**) Summary of the mutation transfer approach. Most ChR-variants harboring ChloC- or IC++-mutations showed no photocurrents. In addition, of constructs, which produced a photocurrent, the majority had no or only partial Cl^- conductivity ($\sigma(Cl^-)$). For details and ChR abbreviations, please see main text. (**C**) Action spectra of aACRs. Peak wavelengths (indicated above) were obtained from fitting with a 3-parameter Weibull distribution. In addition to typical low intensity action spectra (solid lines) obtained with 10 ms pulsed activation, a spectrum with continuous illumination of 500 ms and tenfold increased photon irradiance was recorded for Aurora (dotted line). Data points show mean±SEM (n = 6) Phobos, 9 iC++, 7 Aurora, 6 Aurora with tenfold photon irradiance, 6 iChloC). (**D** and **E**) Typical photocurrent traces at high extracellular [Cl^-] of the newly developed aACRs Phobos (D, right) and Aurora (E) compared to the established aACR iC++ (D, left). The holding potential was increased from -80 mV (bottom) to +40 mV (top trace) in 20 mV steps. Duration of light application at respective wavelengths is indicated by colored bars above the traces.

Figure 2: Kinetics, light sensitivity and control of aACRs. (**A**) Normalized photocurrent traces after light shutoff are displayed for fast cycling aACRs and their respective C128A step-function variants logarithmically binned to 50 data points per decade. (**B**) Light titration of aACRs and aACR C128A variants. Stationary photocurrents are normalized to the maximum (n = 5 Phobos, 4 $Phobos^{CA}$, 7 iC++, 6 $iC{+}{+}^{CA}$, 5 Aurora, 5 Aurora 590 nm, 4 $Aurora^{CA}$, 5 iChloC, 4 $iChloC^{CA}$). (**C**) Light-activation EC_{50} values of fast cycling aACRs (WT) and their C128A variants (CA) obtained from fitted measurements shown in (B). (**D**) Example recording demonstrating the strategy to determine wavelength dependent inactivation for step-function aACRs. After fully opening the channel with a 10 ms light pulse at the peak activating wavelength, light with different wavelengths at identical photon irradiance was applied to accelerate channel closing. The aACR was fully closed with high-intensity red-shifted light after each trial. (**E**) Inactivation spectra calculated from measurements as shown

bioRxiv preprint doi: https://doi.org/10.1101/156422; this version posted June 27, 2017. The copyright holder for this preprint (which was not certified by peer review) is the author/funder. All rights reserved. No reuse allowed without permission.

in (D). Positive values show additional activation, whereas negative values denote inactivation (n = 4 Phobos^{CA}, 6 iC++^{CA}, 5 Aurora^{CA}, 5 iChloC^{CA}). Wavelengths yielding maximal activation and inactivation are displayed for each aACR C128A above or under the curves, respectively. (**F**) Apparent closing kinetic time constants (τ_{off}) of fast cycling aACRs (WT), their C128A variants (CA) and the accelerated closing by application of red-shifted light. (n = 6 Phobos, 4 Phobos^{CA}, 5 Phobos^{CA} accelerated, 8 iC++, 7 iC++^{CA}, 7 iC++^{CA} accelerated, 8 Aurora, 5 Aurora^{CA}, 5 Aurora^{CA} accelerated, 7 iChloC, 5 iChloC^{CA}, 8 iChloC^{CA} accelerated). (**G**) Typical photocurrent traces of the newly developed step-function aACRs Phobos^{CA}, iChloC^{CA} and Aurora^{CA} compared to the established step-function aACR iC++^{CA} (alias SwiChR++), activated by short 10 ms light pulses. Channel closing was always facilitated with red-shifted light. Mean values ± SEM together with single measurement data points (dots) are shown in (B, C, E and F).

Figure 3: Membrane targeting, amplitudes and reversal potentials of aACRS. (**A**) HEK cells expressing the established aACRs iC++, iChloC and their C128A variants or the newly generated aACR Phobos and Aurora and their C128A variants fused to the mCherry were co-labelled with the membrane dye Vybrant®-DiO (middle row). Upper row: confocal images of mCherry, lower row: merged images of aACR-mCherry and labelled cell membrane (equatorial z-slices). Intensity and/or contrast for DiO were adjusted due to different staining efficiency. (**B**) Relative membrane targeting of aACRs (n = 14 Phobos, 12 Phobos^{CA}, 13 iC++, 13 iC++^{CA}, 11 Aurora, 12 Aurora^{CA}, 18 iChloC, 21 iChloC^{CA}). (**C**) Absolute stationary photocurrents of aACRs at indicated conditions (n = 6 Phobos, 5 Phobos^{CA}, 6 iC++, 6 iC++^{CA}, 5 Aurora, 7 Aurora^{CA}, 9 iChloC, 7 iChloC^{CA}). (**E**) Reversal potentials (E_{rev}) for all aACRs at high-extracellular (150 mM) and low-intracellular (10 mM) chloride concentrations (n = 5 Phobos, 5 Phobos^{CA}, 6 iC++, 5 iC++^{CA}, 8 Aurora, 5 Aurora^{CA}, 7 iChloC, 6 iChloC^{CA}). Bar plots show mean±SEM. Single measurement data points are shown as dots.

Figure 4: Phobos and Aurora in CA1 pyramidal cells in organotypic hippocampal slice culture. (**A**) CA1 pyramidal neuron expressing Aurora-Citrine 5 days after electroporation (stitched maximum intensity projections of two-photon images, fluorescence intensity shown as inverted gray values). Citrine fluorescence was mainly localized to the plasma membrane across the entire cell. Inset shows magnified view of the apical dendrite. (**B**) Representative photocurrent traces evoked at indicated wavelengths (10 mW/mm^2). (**C**) Membrane voltage traces in response to 500 ms current injections and 200 ms light pulses at indicated wavelengths (10 mW/mm^2). Light application was delayed by 144 ms with respect to current onset. (**D**) Quantification of action potential inhibition at indicated light intensities and wavelengths (n = 6 to 7). Lines are interpolations of data points and shaded areas represent SEM. (**E** to **H**) same as (A to D) for Phobos-Citrine expressing neurons (H, n = 4 to 7).

bioRxiv preprint doi: https://doi.org/10.1101/156422; this version posted June 27, 2017. The copyright holder for this preprint (which was not certified by peer review) is the author/funder. All rights reserved. No reuse allowed without permission.

Figure 5: iChloC^{CA}, Phobos^{CA} and Aurora^{CA} in CA1 pyramidal cells in organotypic hippocampal slice cultures. (**A**) Representative photocurrent traces of a Phobos^{CA} expressing CA1 cell evoked with different activation wavelengths and shutoff with 595 nm light. (**B**) Photocurrent traces in the same cell evoked with 460 nm light and shutoff with indicated wavelengths (10 mW/mm^2). (**C**) Activation spectra (dashed lines) and inactivation spectra (solid lines) of Phobos^{CA}, iChloC^{CA} and Aurora^{CA} in CA1 pyramidal neurons. Lines are interpolations of data points and shaded areas represent SEM (n = 2 to 9). (**D**) Membrane voltage trace shows reversible suppression of depolarization-induced spiking by photoswitching Phobos^{CA} between open and closed state. (**E** to **G)** Quantification of the spike rate during current injection at indicated time intervals before opening light pulse, after opening light pulse and after closing light pulse in CA1 neurons expressing iChloC^{CA}-Citrine (E, n = 12 neurons in 12 slice cultures), Phobos^{CA}-Citrine (F, n = 7) or Aurora^{CA}-Citrine (G, n = 5). Gray symbols indicate individual experiments. Mean values are shown as rectangular symbols with SEM. ****: $p < 0.0001$, repeated measures one-way ANOVA followed by Tukey's multiple comparisons test.

Figure 6: aACRs in *Drosophila* larval nociception and locomotion. (**A**) Mechano-nociceptive responses (rolling) of 3rd instar larvae after 50 mN stimulation with a *von Frey* filament, with and without light activation of C4da neuron (*ppk-Gal4*) expressed Halorhodopsin (2x eNpHR), iChloC or Aurora. Low light (gray), 470nm (blue) and 525nm (green) conditions are shown as indicated by color (n as indicated, ***: $p < 0.001$, chi^2 test). (**B**) Representative traces of freely locomoting larvae expressing Aurora in motor neurons (*ok371-Gal4*). Arrows indicate onset (green, 525 nm, 21 µW/mm^2) and offset (gray) of light activation. Relative velocity is color intensity coded in red. (**C**) Average larval velocity over time is plotted for Phobos or Aurora expressing animals with activation using a 460 nm or 525 nm light pulse for 15 s, respectively (n = 49 animals for Phobos, n = 52 animals for Aurora, mean ± SEM). (**D** and **E**) Averaged velocity before (5 - 10 s), during (20 - 25 s) and after (35 - 40 s) light induced activation of (D) Phobos or (E) Aurora (n = 49 animals for Phobos, n = 52 animals for Aurora, mean ± SEM). (**F**) Relative velocity reduction during light for Phobos, Aurora and control animals using 460 nm or 525 nm light, respectively (mean ± SEM, ***: $p < 0.001$, ****: $p < 0.0001$, non-parametric Kruskal-Wallis test followed by Dunn's multiple comparisons test). (**G**) Inhibition of larval locomotion by Phobos^{CA} expression in motor neurons (*ok371-Gal4*). Average larval velocity over time showing inhibition of locomotion after light induced Phobos^{CA} activation (460 nm, 80 µW/mm^2) and recovery by channel closing with 595 nm light (1.7 mW/mm^2). All animals on an agar plate were sequentially illuminated (5 s each) for channel closing during the time period indicated by the dashed box. (**H**) Average velocities before (5 - 10 s) light induced activation of Phobos^{CA}, during inhibition (20 - 25 s) and after channel closing with red-shifted 595 nm light (>60 s) (n

bioRxiv preprint doi: https://doi.org/10.1101/156422; this version posted June 27, 2017. The copyright holder for this preprint (which was not certified by peer review) is the author/funder. All rights reserved. No reuse allowed without permission.

= 54 animals, mean ± SEM). (**I**) Comparison of relative larval body size change after $ChR2^{XXL}$ mediated activation of motor neurons and $Phobos^{CA}$ mediated inhibition. Normalized larval body area is plotted over time with indicated light activation of $Phobos^{CA}$ or $ChR2^{XXL}$. (**J**) Quantitative comparison of the relative area change before and after light mediated activation of $ChR2^{XXL}$ or $Phobos^{CA}$ (n = 44 animals for $Phobos^{CA}$, n = 46 animals for $ChR2^{XXL}$, mean±SEM).

Figure 1

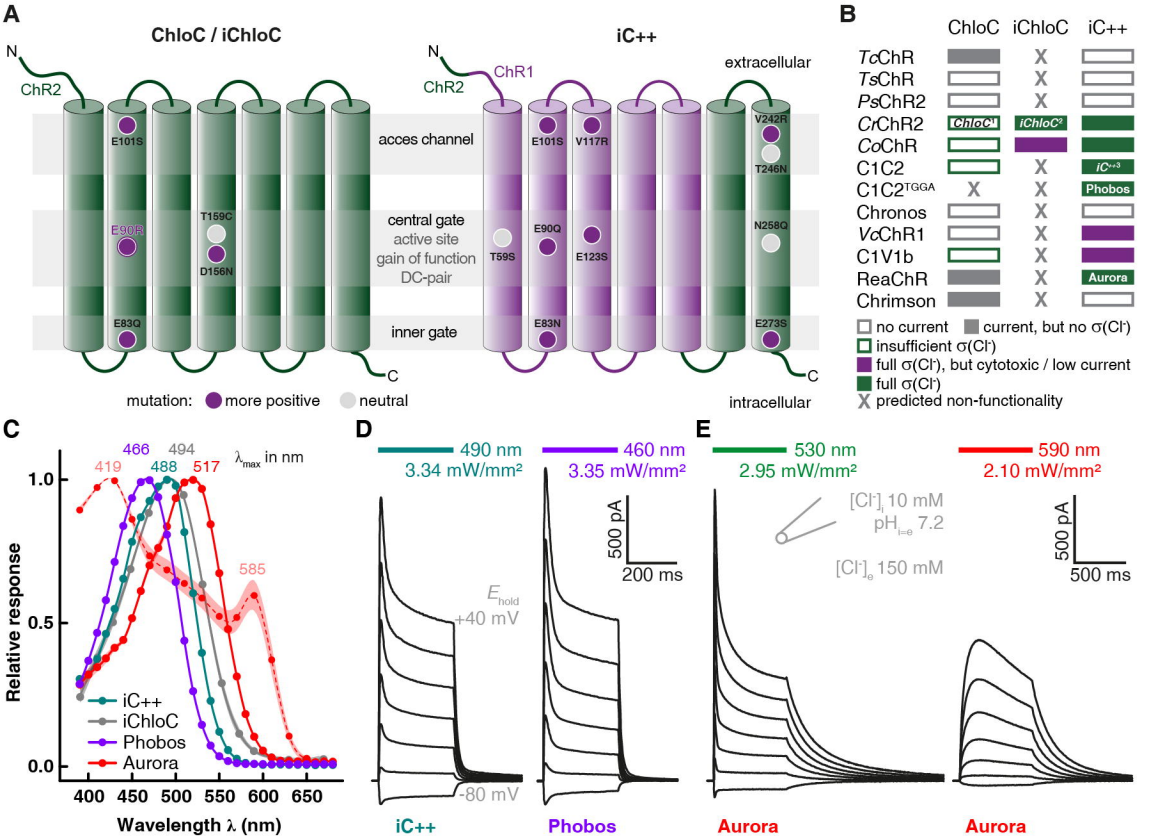
A
ChloC / iChloC
iC++
N
ChR2
ChR1
extracellular
intracellular
acces channel
central gate
active site
gain of function
DC-pair
inner gate
E101S
E90R
T159C
D156N
E83Q
V117R
T59S
E90Q
E123S
E83N
V242R
T246N
N258Q
E273S
C
mutation: more positive neutral
B
ChloC iChloC iC++
TcChR
TsChR
PsChR2
CrChR2
CoChR
C1C2
C1C2TGGA
Chronos
VcChR1
C1V1b
ReaChR
Chrimson
ChloC1
iChloC2
iC++3
Phobos
Aurora
no current
current, but no σ(Cl-)
insufficient σ(Cl-)
full σ(Cl-), but cytotoxic / low current
full σ(Cl-)
X predicted non-functionality
C
λmax in nm
466 494 419 488 517 585
Relative response
iC++
iChloC
Phobos
Aurora
Wavelength λ (nm)
D
490 nm 3.34 mW/mm²
460 nm 3.35 mW/mm²
500 pA
200 ms
Ehold
+40 mV
-80 mV
iC++
Phobos
E
530 nm 2.95 mW/mm²
590 nm 2.10 mW/mm²
[Cl-]i 10 mM
pHi=e 7.2
[Cl-]e 150 mM
500 pA
500 ms
Aurora
Aurora

Figure 2

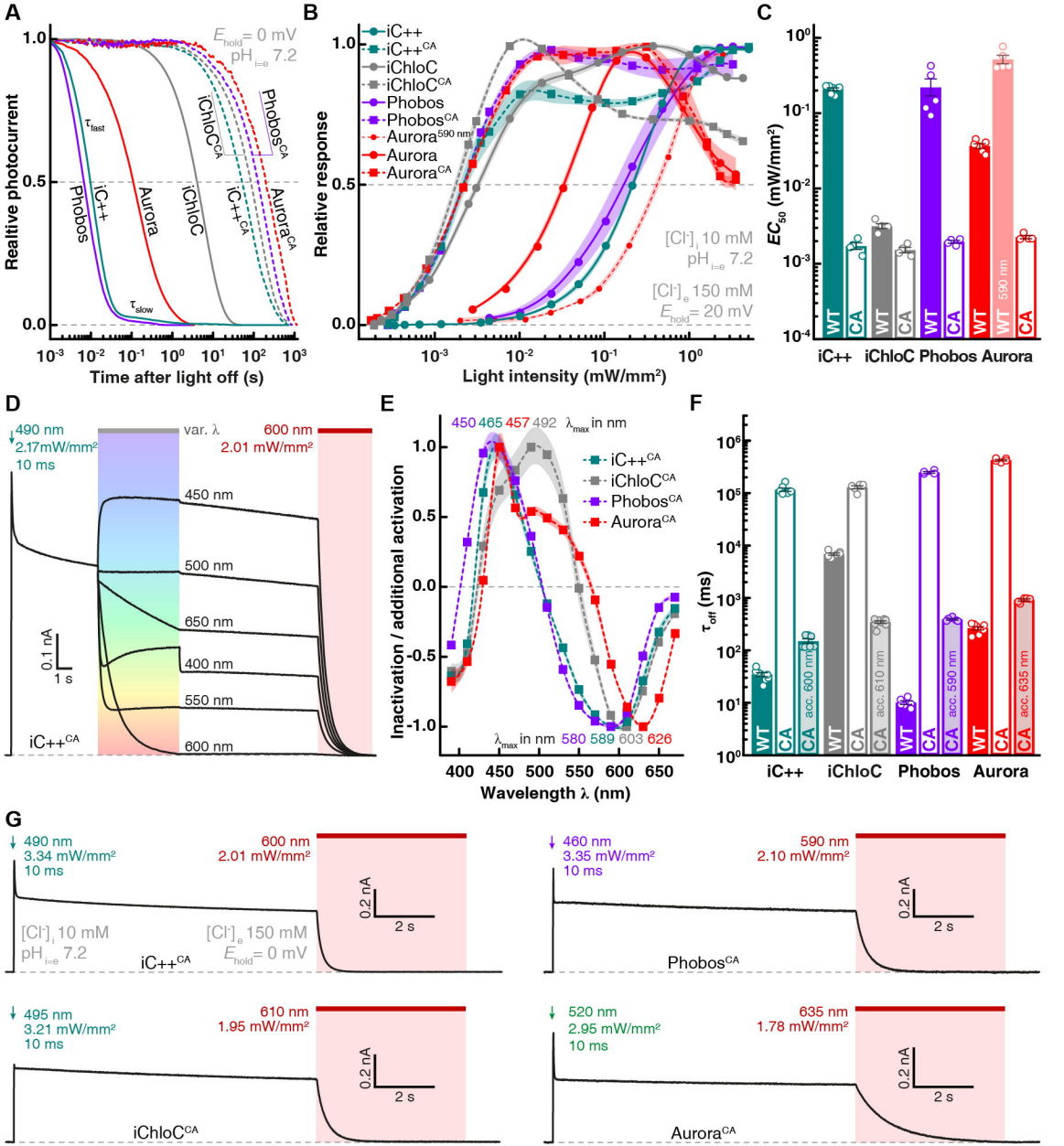
A
Realtive photocurrent
Time after light off (s)
E_{hold} = 0 mV
pH$_{i=e}$ 7.2
τ_{fast}
τ_{slow}
Phobos
iC++
Aurora
iChloC
iChloC^{CA}
iC++^{CA}
Aurora^{CA}
Phobos^{CA}
B
Relative response
Light intensity (mW/mm²)
iC++
iC++^{CA}
iChloC
iChloC^{CA}
Phobos
Phobos^{CA}
Aurora$^{590\ nm}$
Aurora
Aurora^{CA}
[Cl⁻]$_i$ 10 mM
pH$_{i=e}$ 7.2
[Cl⁻]$_e$ 150 mM
E_{hold} = 20 mV
C
EC_{50} (mW/mm²)
WT
CA
590 nm
iC++
iChloC
Phobos
Aurora
D
490 nm
2.17mW/mm²
10 ms
var. λ
600 nm
2.01 mW/mm²
450 nm
500 nm
650 nm
400 nm
550 nm
600 nm
0.1 nA
1 s
iC++^{CA}
E
450 465 457 492 λ_{max} in nm
Inactivation / additional activation
Wavelength λ (nm)
iC++^{CA}
iChloC^{CA}
Phobos^{CA}
Aurora^{CA}
λ_{max} in nm 580 589 603 626
F
τ_{off} (ms)
WT
CA
acc. 600 nm
acc. 610 nm
acc. 590 nm
acc. 635 nm
iC++
iChloC
Phobos
Aurora
G
490 nm
3.34 mW/mm²
10 ms
600 nm
2.01 mW/mm²
0.2 nA
2 s
[Cl⁻]$_i$ 10 mM
pH$_{i=e}$ 7.2
[Cl⁻]$_e$ 150 mM
E_{hold} = 0 mV
iC++^{CA}
460 nm
3.35 mW/mm²
10 ms
590 nm
2.10 mW/mm²
Phobos^{CA}
495 nm
3.21 mW/mm²
10 ms
610 nm
1.95 mW/mm²
iChloC^{CA}
520 nm
2.95 mW/mm²
10 ms
635 nm
1.78 mW/mm²
Aurora^{CA}

Figure 3

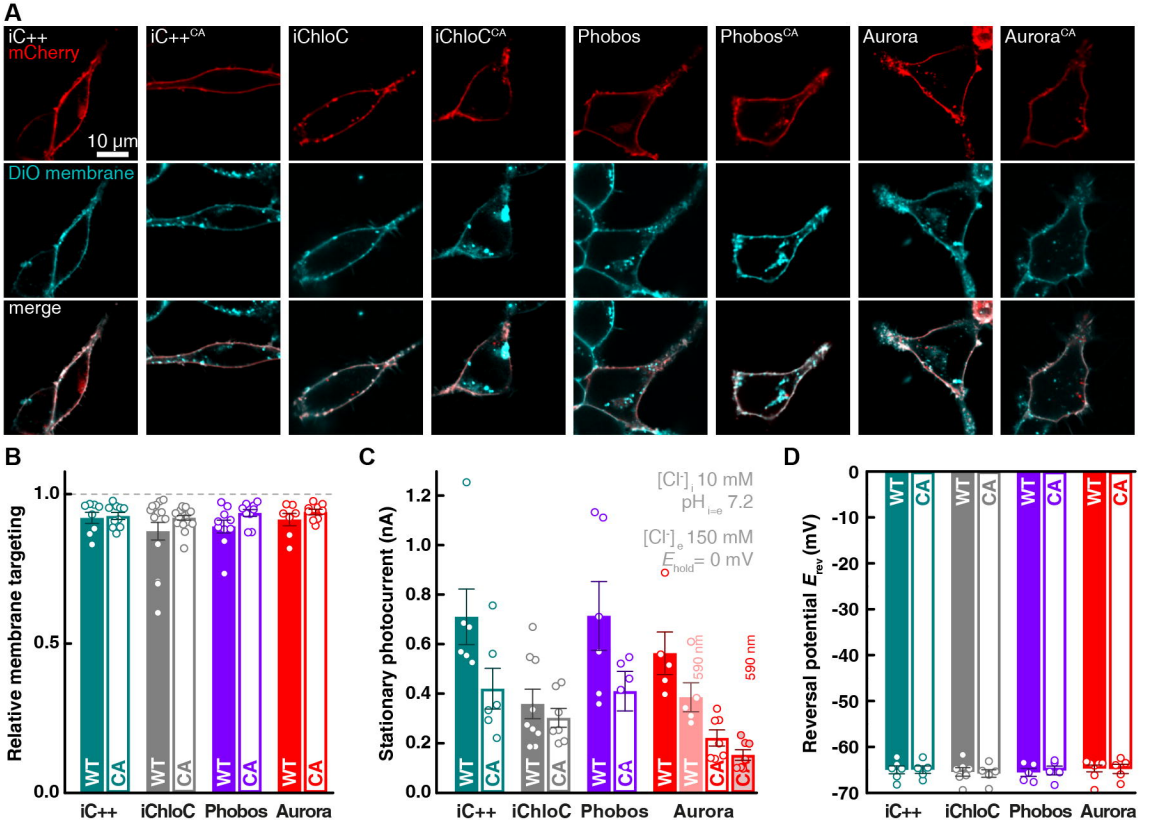
A
iC++
mCherry
10 µm
iC++CA
iChloC
iChloCCA
Phobos
PhobosCA
Aurora
AuroraCA
DiO membrane
merge
B
Relative membrane targeting
1.0
0.5
0.0
WT
CA
iC++
iChloC
Phobos
Aurora
C
Stationary photocurrent (nA)
[Cl-]i 10 mM
pHi=e 7.2
[Cl-]e 150 mM
Ehold = 0 mV
590 nm
D
Reversal potential Erev (mV)
0
-10
-20
-30
-40
-50
-60
-70

Figure 4

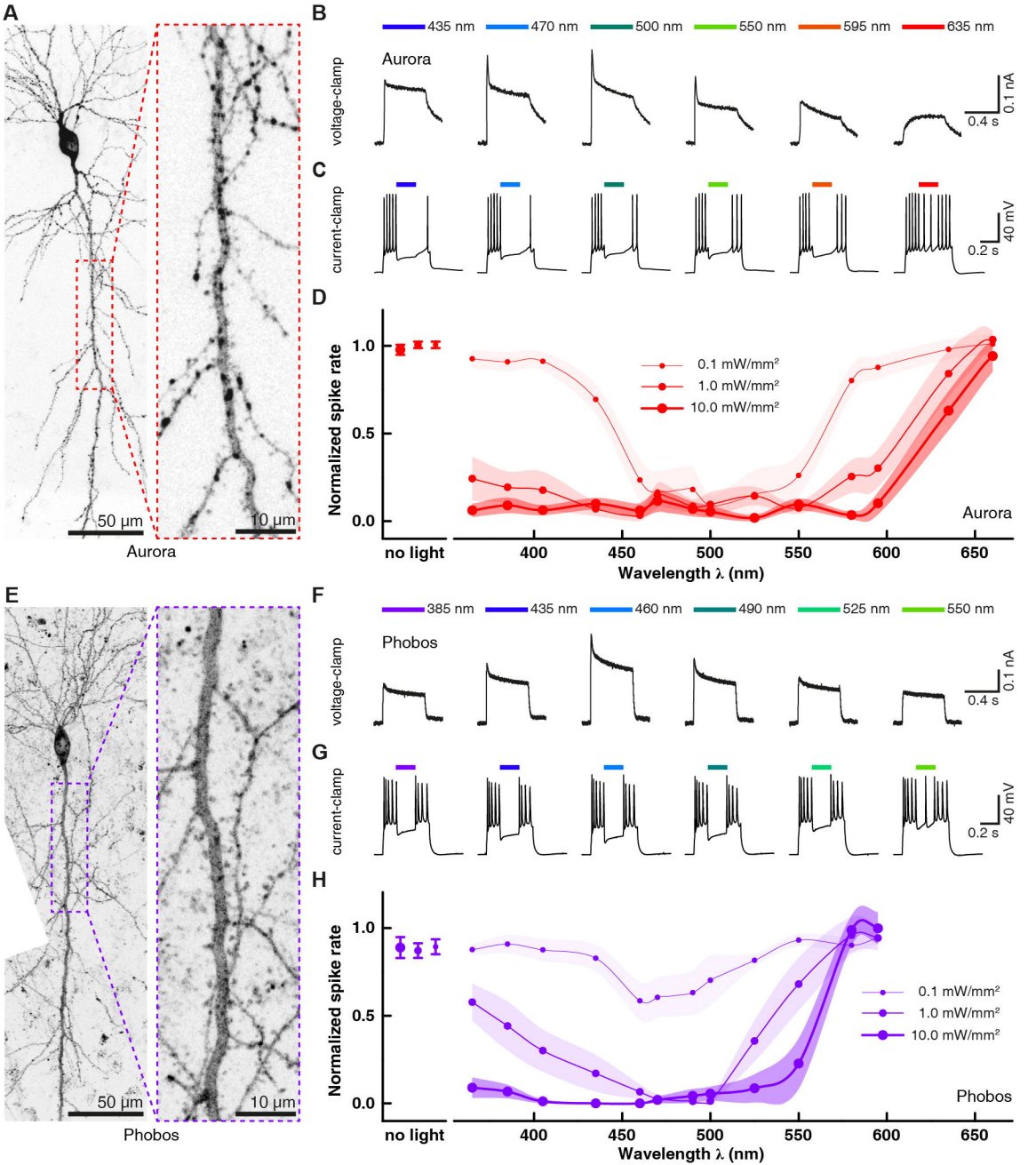
A
50 µm
10 µm
Aurora
B
435 nm
470 nm
500 nm
550 nm
595 nm
635 nm
Aurora
voltage-clamp
0.1 nA
0.4 s
C
current-clamp
40 mV
0.2 s
D
Normalized spike rate
1.0
0.5
0.0
0.1 mW/mm²
1.0 mW/mm²
10.0 mW/mm²
Aurora
no light
400
450
500
550
600
650
Wavelength λ (nm)
E
50 µm
10 µm
Phobos
F
385 nm
435 nm
460 nm
490 nm
525 nm
550 nm
Phobos
voltage-clamp
0.1 nA
0.4 s
G
current-clamp
40 mV
0.2 s
H
Normalized spike rate
1.0
0.5
0.0
0.1 mW/mm²
1.0 mW/mm²
10.0 mW/mm²
Phobos
no light
400
450
500
550
600
650
Wavelength λ (nm)

Figure 5

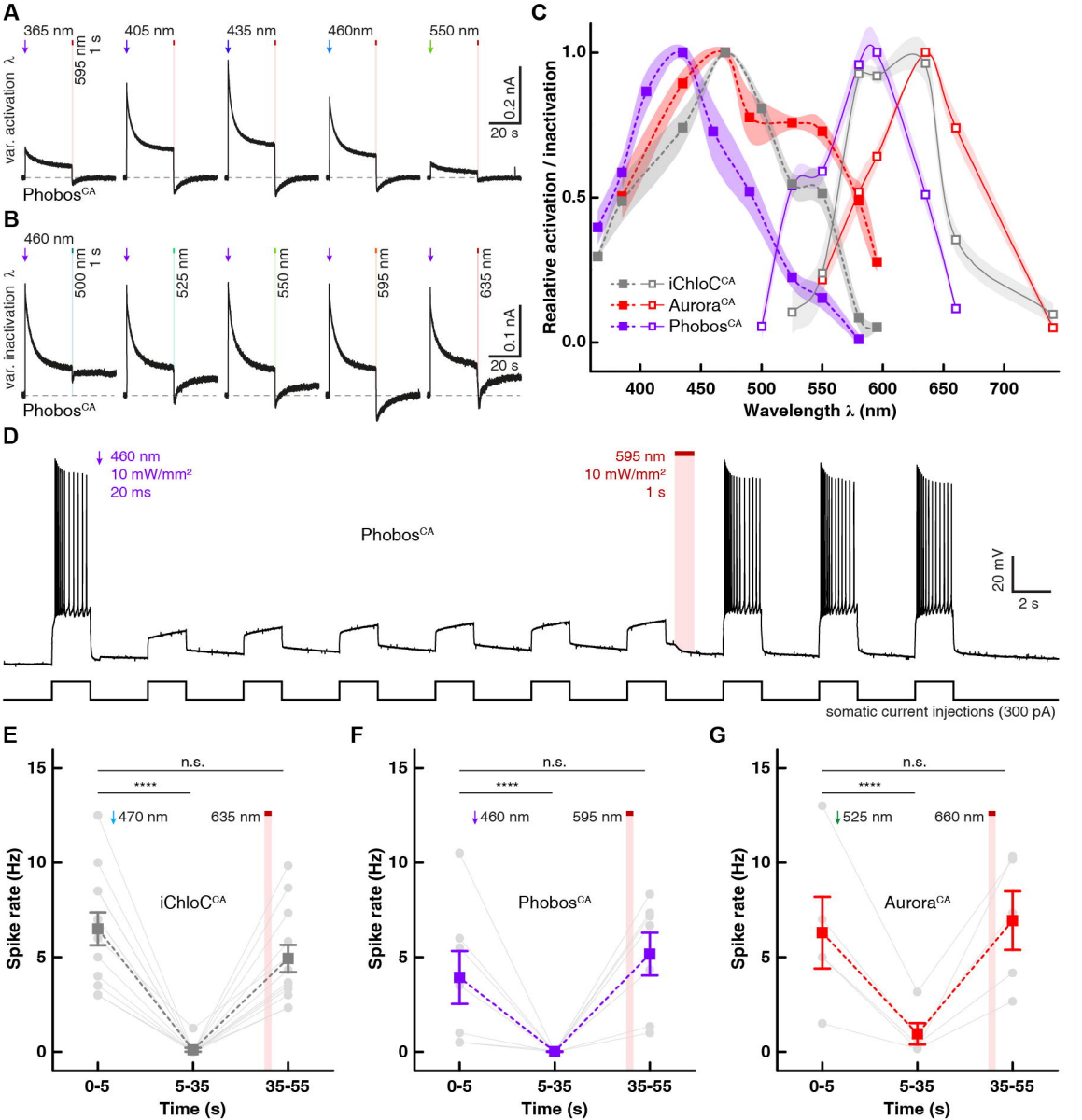
A
365 nm
405 nm
435 nm
460nm
550 nm
595 nm
1 s
var. activation λ
0.2 nA
20 s
PhobosCA
B
460 nm
500 nm
525 nm
550 nm
595 nm
635 nm
var. inactivation λ
0.1 nA
C
Realative activation / inactivation
Wavelength λ (nm)
iChloCCA
AuroraCA
PhobosCA
D
460 nm
10 mW/mm²
20 ms
595 nm
10 mW/mm²
1 s
20 mV
2 s
somatic current injections (300 pA)
E
470 nm
635 nm
iChloCCA
F
460 nm
595 nm
PhobosCA
G
525 nm
660 nm
AuroraCA
n.s.
****
Spike rate (Hz)
Time (s)
0-5
5-35
35-55

Figure 6

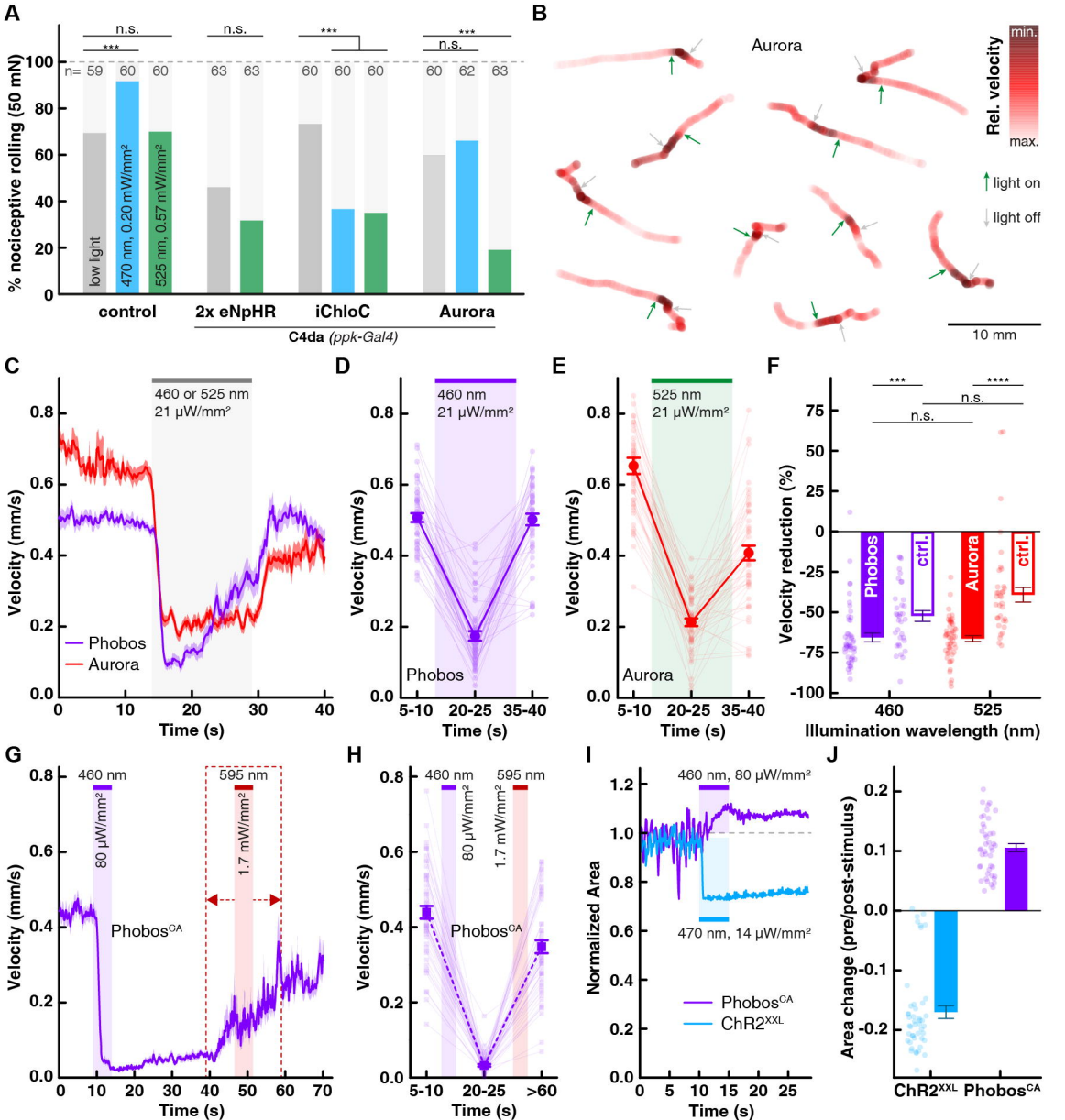
A
% nociceptive rolling (50 mN)
n.s.
***
n.s.
***
n.s.
***
n= 59 60 60 63 63 60 60 60 60 62 63
low light
470 nm, 0.20 mW/mm²
525 nm, 0.57 mW/mm²
control
2x eNpHR
iChloC
Aurora
C4da (ppk-Gal4)
B
Aurora
Rel. velocity
min.
max.
light on
light off
10 mm
C
460 or 525 nm
21 µW/mm²
Velocity (mm/s)
Phobos
Aurora
Time (s)
D
460 nm
21 µW/mm²
Phobos
5-10
20-25
35-40
E
525 nm
21 µW/mm²
Aurora
F
Velocity reduction (%)
Phobos
ctrl.
Aurora
ctrl.
460
525
Illumination wavelength (nm)
G
460 nm
595 nm
80 µW/mm²
1.7 mW/mm²
Phobos^CA
H
>60
I
460 nm, 80 µW/mm²
470 nm, 14 µW/mm²
Normalized Area
Phobos^CA
ChR2^XXL
J
Area change (pre/post-stimulus)
ChR2^XXL
Phobos^CA